frontiers

Time-Scales of Inter-eruptive Volcano Uplift Signals: Three Sisters Volcanic center, Oregon (USA)

Sara Rodríguez-Molina [1], **Pablo J. González** [(2,3)*], **María Charco** [1], **Ana M. Negredo** [1,4] **and David A. Schmidt** [5]

[1] *Instituto de Geociencias (IGEO, CSIC, UCM), C/ Dr. Severo Ochoa 7, 28040 Madrid, Spain*
[2] *COMET. Department of Earth, Ocean and Ecological Sciences, School of Environmental Sciences, University of Liverpool, Jane Herdman Building, 4 Brownlow Street, L69 3GP, Liverpool, United Kingdom*
[3] *Volcanology Research Group, Department of Life and Earth Sciences, Instituto de Productos Naturales y Agrobiología (IPNA-CSIC), 38206 La Laguna, Tenerife, Canary Islands, Spain*
[4] *Dpto. Física de la Tierra y Astrofísica, Facultad de Ciencias Físicas, Plaza de Ciencias 1, Universidad Complutense de Madrid, 28040 Madrid, Spain*
[5] *Department of Earth and Space Sciences, University of Washington, 15th Avenue NE Seattle, WA, United States*

Correspondence*:
Pablo J. González
pjgonzal@liverpool.ac.uk

ABSTRACT

A classical inflation-eruption-deflation cycle of a volcano is useful to conceptualize the time-evolving deformation of volcanic systems. Such a model predicts accelerated uplift during pre-eruptive periods, followed by subsidence during the co-eruptive stage. Some volcanoes show puzzling persistent uplift signals with minor or no other geophysical or geochemical variations, which are difficult to interpret. Such temporal behaviors are usually observed in large calderas (e.g, Yellowstone, Long Valley, Campi Flegrei, Rabaul), but less commonly for stratovolcanoes. Volcano deformation needs to be better understood during inter-eruptive stages, to assess its value as a tool for forecasting eruptions. Here, we analyse inter-eruptive uplift signals at Three Sisters, a complex stratovolcano in Oregon (USA), which in recent decades shows persistent inter-eruptive uplift signals without associated eruptive activity. Using a Bayesian inversion method, we re-assessed the source characteristics (magmatic system geometry and location) and its uncertainties. Furthermore, we evaluate the most recent evolution of the surface deformation signals combining both GPS and InSAR data through a new non-subjective linear regularization inversion procedure to estimate the 26 year-long time-series. Our results constrain the onset of the Three Sisters volcano inflation to be between October 1998 and August 1999. In the absence of new magmatic inputs, we estimate a continuous uplift signal, at diminishing but detectable rates, to last for few decades. Finally, we compare Three Sisters volcano time series with historical

uplift at different volcanic systems. Proper modeling of scaled inflation time series indicates a unique and well-defined exponential decay in temporal behaviour. Such evidence supports that this common temporal evolution of uplift rates could be a potential indicator of a rather reduced set of physical processes behind inter-eruptive uplift signals.

Keywords: Inter-eruptive deformation, characteristic relaxation time, CGPS, InSAR, Geodetic time series, Three Sisters volcano

1 INTRODUCTION

Many volcanoes follow a common deformation pattern consisting of uplift during inter-eruptive periods and subsidence in co-eruptive stages, occasionally interrupted by periods of quiescence or subsidence. Some other volcanoes do not however exhibit this simple behavior (Biggs and Pritchard, 2017). Part of them show puzzling non-steady persistent uplift signals that can last from days to years with minor or no other geophysical or geochemical variations, which are difficult to interpret. Therefore, uplift during inter-eruptive episodes cannot be only interpreted as a pre-eruptive precursory indicator.

Such temporal behavior is usually observed in large calderas (e.g, Yellowstone, Long Valley, Campi Flegrei, Rabaul), but less commonly for stratovolcanoes. Three Sisters Volcanic Complex, located in the Cascade Range volcanic arc of Oregon (Figure 1), is a good example of a dormant system with persistent inter-eruptive uplift without associated eruptive activity or significant seismicity. In 2001, ERS-1/2 satellite interferometric synthetic aperture data (InSAR) analysis from 1992 to 2000 revealed active uplifting located 6 km west of South Sister (Wicks, 2002). Previous studies (Wicks, 2002; Dzurisin et al., 2006, 2009; Riddick and Schmidt, 2011) show evidence that observed uplift can be described by a spherical point source within an homogeneous isotropic elastic half-space. Nevertheless, deformation source geometry is non-unique and sources as horizontal crack, vertical prolate spheroid, and sill-like have been proposed at Three Sisters to fit geodetic data. Interpretation of the temporal evolution of InSAR, leveling and GPS data suggests the beginning of deformation in late 1997 or 1998, with a maximum uplifting rate of $3-5 cm/year$ during $1998-2001$. Microgravity data collected between $2002-2009$ show no significant change in the mass flux across the deforming area (Zurek et al., 2012). No studies have been published about the uplift evolution over the last decade. The uplift process was still on-going in January 2020, when this manuscript was prepared.

An important goal in volcano eruption forecasting is to find how the deformation time-series can distinguish among physical processes, especially during inter-eruptive periods leading to a pre-eruptive scenario. The latter are characterized by new injections of magma/increment of volatiles, viscoelastic relaxation of the media, or a mixing of different coeval processes. Therefore, we must constrain what controls usually long-lived or persistent uplift at volcanic centers. Le Mével et al. (2015) show that the temporal evolution of deformation surprisingly follows the same pattern for different volcanic systems at specific analyzed periods (Yellowstone, Long Valley, Laguna de Maule and Three Sisters). This is consistent with the hypothesis that similar processes may be at work. After this stage, these volcanoes presented an eventual pause and/or change to subsidence (related to seismic events and/ or hydrothermal changes), but did not produce an eruption.

In this work, we studied the time-scales of inter-eruptive uplifting volcanoes, in particular the Three Sisters deformation time-series. We aimed to determine whether Three Sisters is still inflating, analyzing available continuous GPS data since 2001 and multiple satellite interferometric data spanning the 1993-2020 period. A consistent analysis of the time-evolution and mechanisms underlying the Three Sisters

uplift signal is a challenging task. Therefore, we proposed combining multiple geodetic data-sets using an improved linear regularization method based on Truncated Singular Value Decomposition (TSVD) (González et al., 2013) to find an optimal regularization criteria for Three Sister data-set combination. We obtained a seamless, continuous time series of volume change (and its uncertainties) with which to rigorously assess changes over the 26-year studied period. Finally, we compared the Three Sisters temporal behaviour to other well-known examples of uplifting volcanoes to understand (1) whether a variety or not of physical mechanism are at work behind deformation and, if so, (2) if uplift time-scales are informative of whether a certain volcano is on a late or early stage of the inter-eruptive period.

2 DATA SETS

Geodetic information for Three Sisters volcanic center has been accumulating since the discovery in 2001 of surface deformation, first detected by InSAR (Wicks, 2002). Nowadays, deformation is continuously monitored through GPS. We aim to use all available geodetic data to extend the detailed uplift history to the present (2020).

2.1 Continuous GPS

In May 2001, the U.S Geological Survey (USGS), in collaboration with the U.S. Forest Service, installed a continuous GPS station (HUSB) near the actively deforming area. It was strategically installed at a location approximately $\sim 2\ km$ northwest of the detected uplift center. HUSB is part of the USGS Pacific Northwest Network, so it is automatically processed to obtain daily coordinates. No other regional and local continuous GPS station falls within the deformation area. Hence, the HUSB time-series is particularly important to understand the surface deformation time-scales at Three Sisters.

Daily GPS data (coordinates and their uncertainties) are analyzed by the USGS using GIPSY/OASIS II software. Common-mode daily biases are estimated and removed using QOCA (Dzurisin et al., 2009). Three Sisters is located near the actively deforming Cascadia margin, so any geodetic data and coordinates must consider the wider regional deformation patterns. The motion of a background steady rigid-body motion with a rotation pole situated near the eastern limit of Oregon must therefore be removed from the time-series, and a correction for predicted horizontal tectonic motion should be applied. Here, we remove a linear trend of 4.29 mm/yr for the North component and 1.50 mm/yr for the East component. This model prediction represents an update and improved version of the horizontal displacements at HUSB (Dzurisin et al., 2006, 2009; M. Lisowsky personal communication, Cascades Volcano Observatory, 2017).

Figure 2 shows the resulting GPS displacements between July 2001 and January 2020. CGPS data reveals several gaps that occurred due to snowfall in the winter seasons. Furthermore, CGPS shows a gap and a posterior data offset during August 2017-August 2018. USGS data site reports some readjustment of HUSB permanent station during this period and these could explain some of the gaps and offsets in the time series.

2.2 Interferometric Synthetic Aperture Radar (InSAR)

Our InSAR data set includes 85 interferometric pairs, with temporal baselines from 35 to 2894 days, from four satellite missions (ERS, ENVISAT, ALOS-1 and Sentinel-1). ERS and ENVISAT SAR images were acquired during summer and fall between 1993 and 2010 (descending orbits, tracks 113 and 385; ERS and ENVISAT look angles 20.2° and 19.8°, respectively). We used 51 interferograms processed with the ROI PAC software (Rosen et al., 2004) and unwrapped using SNAPHU (Chen and Zebker, 2002), with perpendicular baselines up to 500 m, as explained by Riddick and Schmidt (2011).

To improve the temporal coverage of InSAR observations, we also analyzed data from the ALOS-1 and Sentinel-1 SAR data missions. The mean line-of-sight velocity of ALOS-1 data (path 219, ascending orbit, look angle 38.7°) was obtained during January 2007- March 2011. Most individual interferograms in the Cascades range show poor coherence because of vegetation and seasonal snow coverage, hence we also processed 4 Sentinel-1 summer-to-summer and summer-to-late spring interferometric pairs, between September 2015 and May 2018, for descending (path 115, look angle 39.8°) and ascending (path 137, look angle 38.8°) orbits. To provide deformation data during the GPS gap mentioned above, two Sentinel-1 interferometric pairs cover that period (Figure 6). We used JPL InSAR Scientific Computing Environment (ISCE) software (Rosen et al., 2012), processing Level-0 raw ERS-1 and ALOS-1, and SLC-level Sentinel-1 radar data. All interferograms were corrected for orbital and topographic contributions using precise orbit information and the SRTM digital elevation model (Farr et al., 2007). We also reprocessed a highly coherent interferometric pair for ERS-1 track 365 (descending orbit, corresponding to August 1997 - September 2000). This interferogram was essential to further re-evaluate the magmatic source location and constrain its uncertainties.

L-band data (wavelength $\sim 24\ cm$) from ALOS-1 was very useful to avoid decorrelation owing to the vegetation encompassing the Three Sisters area. Although the LOS deformation rate from 2006 to 2010 is small (about $6-8\ mm/yr$) making it difficult for a single L-band interferogram to detect the deformation signal (Riddick and Schmidt, 2011), a cumulative LOS deformation time-series can detect such changes in rate. The corresponding time-series was processed by StaMPS Version 3.3.b1 to study the surface deformation, applying the Small Baselines method for 30 interferometric pairs (Hooper et al., 2012; Bekaert et al., 2017). Small Baselines method minimizes decorrelation in natural terrains. So, it is an appropriate method for the Three Sisters area, which lacks man-made structures and hence offers few dominant persistent scatterers.

Due to the small deformation rate (5.8 $mm/year$ for the period June 2015 - January 2020) and low signal-noise ratio in the Cascades, geodetic data must be analyzed carefully (Poland et al., 2017). Following this recommendation, we consider a 1 cm standard deviation for neighboring pixels in all interferograms. Only four good quality interferometric pairs were used for the Sentinel-1 observation period. Adding more interferograms did not significantly improve the analysis of the volume change time-series. Moreover, the analysis of a 6-year long Sentinel-1 dataset in Turkey indicates that surface displacement rate uncertainties are mostly dominated by length of observation, rather than larger numbers of available interferograms (Weiss et al., 2020). Hence, we consider Sentinel-1 summer-to-summer and summer-to-late spring InSAR data to avoid decorrelation due to snow coverage, and to fill a noticeable GPS time-series gap. However, the deformation rates could be reexamined in future, using longer Sentinel-1 datasets.

Figure 3 represents the mean LOS velocity ($mm/year$) for the ascending path 219 ALOS-1 from January 2007 to March 2011. Due to the high signal-to-noise ratio, the StaMPS LOS velocity results were noisy and

we post-processed them to reduce undesirable oscillations of non-volcanic origin. We applied a band pass filter to retain spatial deformation signals between 10 and 0.8 km, using a median filter (GMT blockmedian). Although close to the signal-to-noise ratio value, results indicate a $6\,km$ circular uplift pattern west of South Sister with a mean LOS velocity of approximately $5-10\,mm/year$. This mean velocity is consistent with a value obtained for the HUSB CGPS station during the same period ($5.2\,mm/year$).

3 MODELING

Here, we introduce a mathematically rigorous strategy for the joint inversion of time-dependent InSAR (different look angles and sensors, high spatial resolution) and continuous GPS (daily sampling) data to achieve a complete timeline of volcanic activity and quantify a single time series of volume flux rates. The strategy captures the benefits of each system avoiding the time evolution determination on a point-by-point basis. It is based on the two-step approach proposed by González et al. (2013) that produces time series of volume from sets of different look angles and satellite sensors once an active source is determined for an inflation period. In this section, we provide a description of the González et al. (2013) algorithm and extent it (1) to include continuous GPS data and therefore to combine different components and/or look vectors using a unique source model and (2) to afford a defined method of truncation of the TSVD technique used to regularize the inverse problem, with the goal of finding the time evolution of volume and therefore to improve the accuracy on the estimation of volume time series. First, we show how the active source location (horizontal position and depth) and geometry is determined using a Bayesian inversion approach. Subsequently, we solve for temporal evolution of volume.

3.1 Source Characterization

First of all, we optimized the active magmatic source through a Bayesian inversion, using InSAR data spanning the period of maximum displacement. The horizontal location, depth and geometry of the inflation source at Three Sisters was computed using the MATLAB®-based software package GBIS (Geodetic Bayesian Inversion Software) (Bagnardi and Hooper, 2018), which estimates source parameters through a Markov chain Monte Carlo method and uses, among others, analytical forward models from dMODELS software package (Battaglia et al., 2013). It obtains the posterior probability distributions (PDFs) for all model parameters by taking into account uncertainties in the data (e.g., data errors). To achieve this, considering the pattern of surface deformation, we employ simple elastic models such as point spherical (Mogi, 1958), prolate spheroid (Yang et al., 1988) and sill-like (Fialko et al., 2001) models. An elastic, homogeneous and isotropic half-space is assumed in all the approaches with Poisson's ratio 0.25. We assumed, as previous studies (Dzurisin et al., 2006, 2009; Riddick and Schmidt, 2011), an stationary source and we used an interferogram spanning August 1997 - September 2000 to look for source parameters. This interferogram fulfills two important conditions to determine the best-fitting static displacements: (1) it spans the shortest time during the period of maximum deformation;(2) it shows acceptable signal-to-noise ratio. InSAR spatially correlated error (caused mainly by the "wet" tropospheric delay) is estimated by modeling experimental semivariograms in deformation-free regions (Bagnardi and Hooper, 2018). InSAR data is subsampled with an adaptative quadtree method (Decriem et al., 2010) to reduce the computational cost of the Bayesian inversion, particularly for a sill-like source. The inversion computes $2 \cdot 10^6$ iterations

for spherical point and $5 \cdot 10^6$ iterations for prolate spheroid and sill-like sources, which stabilizes the inversion procedure.

3.2 Temporal Evolution of the Source Volume Changes.

Once the magmatic system is fixed, we perform the quasi-dynamic time-dependent model using a linear inversion scheme to look for the volume changes at each interferogram's period and the cumulative volume changes since the first GPS observation. Both, volume changes at each interferogram and cumulative volume changes from the GPS data are used to solve for the time evolution of volume using TSVD.

3.2.1 First step: Piecewise volume changes over temporal data periods

Once the location and geometry of the inflation source are fixed, we determine the volume changes over the corresponding time intervals (increments of volume changes, ΔV) for both, InSAR and CGPS data sets, which are assumed to be uncorrelated. In this way, observations from several interferograms and GPS sites can be combined to estimate increments of volume changes assuming a unique source model. Each volume change, ΔV_{ij}, records (1) the incremental volume change between two acquisition dates, t_i and t_j from an interferogram or (2) the cumulative increment of volume since the first observation, i.e., $t_j = t_0$, being t_0 the starting date of CGPS.

A linear inversion scheme using Weighted Least Squares (WLS, Menke, 1989) is applied. The inversion is constrained by 55 interferometric pairs (ERS, ENVISAT, Sentinel-1), one ALOS-1 interferogram (cumulative LOS deformation time-series) and a 3-component GPS time series. The forward problem is defined by $\mathbf{d} = \mathbf{Gm}$, where $\mathbf{d}$ is the data vector (InSAR or GPS), $\mathbf{m}$ is the model parameter ($\Delta\mathbf{V}$) vector, and $\mathbf{G}$ is the Green's function matrix representing the impulse response for the specific elastic source, projected into the three components of GPS or the satellite line-of-sight. Therefore, a total of 5064 independent linear inversions were performed to find the increments of volume changes, ΔV_{ij}, given the set of interferograms and 5008 cumulative GPS displacements.

The least square estimator of each inversion, $\hat{\mathbf{m}}$, is given by:

$$\hat{\mathbf{m}} = \left[\mathbf{G}^T {\mathbf{C_d}}^{-1} \mathbf{G}\right]^{-1} \mathbf{G}^T {\mathbf{C_d}}^{-1} \mathbf{d}, \tag{1}$$

with the cofactor matrix $\mathbf{C}_{\hat{\mathbf{m}}} = \left[\mathbf{G}^T {\mathbf{C_d}}^{-1} \mathbf{G}\right]^{-1}$. We considered a diagonal variance-covariance matrix, $\mathbf{C_d}$, assuming that all data are independent, which significantly reduces the computation time of the inversions. Hence, we ignore the possible spatial and temporal correlation noise in InSAR data (e.g., pixel correlation due to atmospheric artifacts, topography structures, repeated acquisitions) and between GPS components (Biggs et al., 2010; Lohman and Simons, 2005).

3.2.2 Second step: Volume Changes Time-series

We want to solve for the temporal evolution of volume change for each observed epoch t_k from ΔV_{ij} obtained on first step considering both InSAR and CGPS data. Instead of volume change itself, the rate of volume changes is inverted as a function of time by applying the Short Baseline Subset Approach (SBAS, Berardino et al., 2002). This prevents the presence of large discontinuities in the final solution.

Let $\Delta\mathbf{V}$ be the data vector of volume changes over the corresponding time intervals $(N \times 1)$, and $\dot{\mathbf{V}}$ the unknown vector of volume change rates $(M \times 1)$ between adjacent epochs, t_j where the overdot means differentiation over time. Then,

$$\dot{\mathbf{V}} = \begin{bmatrix} \dot{v_1} = \frac{v_1}{t_1 - t_0} \\ \vdots \\ \dot{v_M} = \frac{v_M - v_{M-1}}{t_M - t_{M-1}} \end{bmatrix}. \tag{2}$$

The usual method of converting the observations $\Delta\mathbf{V}$ on volume change rates is:

$$\mathbf{B}\dot{\mathbf{V}} = \Delta\mathbf{V}, \tag{3}$$

where $\mathbf{B}$ is the design matrix $(N \times M)$. To determine the components of $\mathbf{B}$, we define a $(M \times 1)$ vector $\mathbf{E}$, containing the single epochs t_j present in all time intervals and sorted in chronological order, for $j = 1, ..., M$; and a $(N \times 2)$ vector $\mathbf{F}$, whose columns are the slave (t_{slave_i}) and master (t_{master_i}) epochs of each i time interval, for $i = 1, ..., N$. Therefore, the (i, j) component of the design matrix is $B_{ij} = (t_{j+1} - t_j)$ for $t_{slave_i} \leq t_j < t_{master_i}$, and zero elsewhere. In the case of cumulative $\Delta\mathbf{V}$ (i.e, continuous GPS), $\mathbf{B}$ presents lower triangular matrix blocks. For example, if volume changes are obtained over different time intervals, i.e., if t_{AB}, t_{BC} and t_{AC} (from InSAR data), and t_{CD}, t_{CE}, t_{CF} (from CGPS data) are Δv_{AB}, Δv_{BC}, Δv_{AC}, Δv_{CD}, Δv_{CE} and Δv_{CF}, the design matrix is given by:

$$\begin{pmatrix} (t_B - t_A) & 0 & 0 & 0 & 0 \\ 0 & (t_C - t_B) & 0 & 0 & 0 \\ (t_B - t_A) & (t_C - t_B) & 0 & 0 & 0 \\ 0 & 0 & (t_D - t_C) & 0 & 0 \\ 0 & 0 & (t_D - t_C) & (t_E - t_D) & 0 \\ 0 & 0 & (t_D - t_C) & (t_E - t_D) & (t_F - t_E) \end{pmatrix} \begin{pmatrix} \dot{v}_{AB} \\ \dot{v}_{BC} \\ \dot{v}_{CD} \\ \dot{v}_{DE} \\ \dot{v}_{EF} \end{pmatrix} = \begin{pmatrix} \Delta v_{AB} \\ \Delta v_{BC} \\ \Delta v_{AC} \\ \Delta v_{CD} \\ \Delta v_{CE} \\ \Delta v_{CF} \end{pmatrix}. \tag{4}$$

To illustrate the simple example in Equation 4 , let all dates, t_A, t_B, t_C, t_D, t_E and t_F be equally spaced at time intervals of 1 year, i.e., $t_{AB} = 1$ year and so on, and $\Delta\mathbf{V} = [2, 1, 3, 1, 2, 3] \times 10^6\ m^3$. In this case, standard least squares can be applied, given $\dot{\mathbf{V}} = [2, 1, 1, 1, 1] \times 10^6\ {}^{m^3}/_{year}$. The cumulative volume times series is then $\mathbf{V} = [2, 3, 4, 5, 6] \times 10^6\ m^3$, meaning a linear inflation rate of $2 \times 10^6\ {}^{m^3}/_{year}$ in time interval t_{AB} and a posterior linear inflation rate of $1 \times 10^6\ {}^{m^3}/_{year}$.

However, the set of ΔV_{ij} forms, in general, an unconnected set of observations with at least one time step not directly related to data, making Equation 4 an ill-posed problem without solution even in the least square sense. Thus, given $\mathbf{P}$ a definite positive matrix, a least-square solution, $\hat{\dot{\mathbf{V}}} = (\mathbf{B}^T\mathbf{P}\mathbf{B})^{-1}\mathbf{B}^T\Delta\mathbf{V}$, is not possible since Equation 4 constitutes an ill-posed unstable model, with one or more eigenvalues of the normal matrix $\mathbf{B}^T\mathbf{P}\mathbf{B}$ close to zero. This fact is responsible for large uncertainty on the estimated volume change rates, $\hat{\dot{\mathbf{V}}}$. Alternatives to the least square method can be proposed for an improved estimate of $\hat{\dot{\mathbf{V}}}$: Tikhonov regularization (Tikhonov and Arsenin, 1977), Bayesian and stochastic inferences (Backus, 1988),

Truncated Singular Value Decomposition (TSVD) or Principal Components (Lawless and Wang, 1976; Hansen, 1990, 1992). Here, we consider TSVD as proposed by González et al. (2013).

3.2.3 Regularized Linear Joint inversion

A key difficulty in applying the TSVD method is how to set up proper criteria to truncate eigenvalues due to the lack of a theoretically solid foundation to discard small nonzero eigenvalues. We developed a strategy to circumvent this difficulty based on Picard condition and L-curve methodology. In such way, we are assured a good balance, filtering out enough noise without losing too much information in the computed solution (Hansen and O'Leary, 1993). Furthermore, we included some estimations of the error of data ($\Delta\mathbf{V}$) to establish some uncertainty in the $\hat{\mathbf{V}}$ estimator. To estimate the uncertainties, the Weighted Generalized Inverse method (Menke, 1989) permitted the use of the "a priori" information from the data $\mathbf{C}_{\Delta\mathbf{V}}$ (and optional model, $\mathbf{C}_{\dot{\mathbf{V}}} = \mathbf{A}^T\mathbf{P}\mathbf{A}$) covariance matrix. Such matrices can be decomposed as:

$$\begin{aligned} \mathbf{C}_{\Delta\mathbf{V}} &= [\mathbf{D}\mathbf{D}^T]^{-1} \\ \mathbf{C}_{\dot{\mathbf{V}}} &= [\mathbf{S}\mathbf{S}^T]^{-1} \end{aligned} \tag{5}$$

where the $\mathbf{D}$ ($N \times N$) and $\mathbf{S}$ ($M \times M$) matrices are determined from the eigenvalue problem of each covariance matrix. In our case, no model covariance information is used, so $\mathbf{C}_{\dot{\mathbf{V}}} = \mathbf{I}$. $\mathbf{C}_{\Delta\mathbf{V}}$ is obtained by error data propagation through $\Delta\hat{\mathbf{V}}$ estimator. The utility of $\mathbf{D}$ and $\mathbf{S}$ is the introduction of a transformed coordinate system where data (and optional model) parameters each have uncorrelated errors and unit variance. Therefore, $\Delta\mathbf{V}_{\mathbf{new}} = \mathbf{D}\Delta\mathbf{V}$, $\dot{\mathbf{V}}_{\mathbf{new}} = \mathbf{S}\dot{\mathbf{V}}$ and $\mathbf{B}_{\mathbf{new}} = \mathbf{D}\mathbf{B}\mathbf{S}^{-1}$ give the transformation of data, model parameters and forward operator in the new system of coordinates. TSVD is applied to $\mathbf{B}_{\mathbf{new}}$ with a specific regularization method to find the Principal Components of the observation set ($\Delta\mathbf{V}$). Then, the problem is back to the original coordinates to achieve the solution and finally, the volume change time-series is obtained by integrating the volume change rate in time:

$$V(t) = \sum \dot{V}\,\delta t \tag{6}$$

3.2.4 Regularization: Techniques used for truncation of small eigenvalues

Some workable criteria for truncation in interdisciplinary problems include L-curve, Discrete Picard condition and Generalized cross validation (GCV) (Hansen, 1992, 2007; Hansen and O'Leary, 1993). Methods like GCV sometimes fail to find the appropriate regularization parameter (flat local minima), whereas the L-curve gives a robust estimation (Hansen and O'Leary, 1993) and the appropriate smoothing solution, which is very attractive from a mathematical point of view. We thus designed a strategy based on a L-curve to set up proper criteria to truncate the eigenvalues.

First, we considered the Discrete Picard condition to explain the instability of the transformed linear inverse problem (Equation 3) and disregarded the smallest singular values (Hossainali et al., 2010; Hansen, 1990, 2007):

$$\left\|\dot{\mathbf{V}} - \dot{\mathbf{V}}_{T_1}\right\|_2 \leq P^{\frac{1}{2}} \max_{1 \leq i \leq M-P} \left\{ \frac{\left|u_i^T \Delta V_i\right|}{s_i} \right\} \tag{7}$$

where $\left\|\dot{\mathbf{V}} - \dot{\mathbf{V}}_{T_1}\right\|_2$ is the regularization error, $\dot{\mathbf{V}}$ and $\dot{\mathbf{V}}_{T_1}$ being the exact and truncated SVD solutions; P is the regularization parameter value, s_i are the singular values, and $\left|u_i^T \Delta V_i\right|$ are called Fourier coefficients (ΔV_i are data and u_i the corresponding eigenvectors of the data space). The Discrete Piccard condition is satisfied if, for all singular values larger than P, the corresponding Fourier coefficients decay faster on average than s_i.

The L-curve method is applied to $\dot{\mathbf{V}}_{T_1}$ resulting in turn from applying (Equation 7) through a log-log plot of the norm of a regularized solution $\left\|\dot{\mathbf{V}}_{T_2}\right\|_2$ versus the norm of the corresponding residual norm $\left\|\mathbf{B}\dot{\mathbf{V}}_{T_2} - \Delta\mathbf{V}\right\|_2$. As recommended by Hansen (1992) we fit the log-log plot of discrete points with some curves, choosing a 2D spline curve and then search for the truncation parameter by computing the L-corner (maximum curvature point). This corner of the spline curve is approximated to the closest discrete point. The L-corner is located exactly where the solution changes in nature from being dominated by regularization errors to being dominated by the residual size. This regularization filters out the contribution of small singular values and noisy data.

4 INVERSION RESULTS

4.1 Re-evaluation of Source Location and Geometry

We performed the Bayesian inversion for spherical point, prolate spheroid and sill-like sources, with similar results. The extra modeling parameters of the prolate spheroid did not improve the misfit. For simplicity, we show only the results corresponding to spherical point and sill-like sources, represented in Figures 4 and 5. Tables 1 and 2 report the PDFs and the 95% credible intervals for all model parameters. The inversion reveals that the surface displacements can be explained by a spherical point source with depth $(4500 - 6000)$ m and ΔV $(7 - 13) \cdot 10^6$ m^3, and with a sill-like source with depth $(5600 - 7200)$ m, radius $(200 - 400)$ m and dimensionless excess pressure $0.06 - 0.30$. The descending ERS Track 385 wrapped interferogram reveals a near axisymmetric deformation pattern, with a maximum LOS surface displacement of ~ 5 cm recorded at the center of the uplifting pattern (Figures 4**A**, **D**). Figures 4**B**, **E** present the predicted spherical point and sill-like forward models, using the median value of the PDF of the model parameters. As expected from the deformation pattern, both are very similar, suggesting that the geometry of the source is far from unique. Therefore, we favor the simplest spherical point source model over a sill-like source, to fit deformation pattern displayed in Figures 4**A** and **D**. Blue stars represent the horizontal location of spherical point and sill-like estimated sources (Tables 1 and 2). Figures 4**C** and **D** show the residuals between observed LOS displacement, and spherical point and sill-like model predicted displacements. The residual is larger close to the Three Sisters complex volcano (green triangles), due to orbital and topographic contributions, and also in the western half of the uplift pattern, where data are less dense.

Figure 5 displays the histograms of marginal PDF for the four spherical point and five sill-like source parameters. Black solid lines show the optimal values for the corresponding model parameters. For the sill-like source, the radius and dimensionless excess pressure PDFs exhibit bi-modality.

4.2 Source Inflation Time-series

We performed a CGPS and InSAR joint inversion to obtain the time-line of volume changes, considering the best fitting source location for the spherical point source geometry to better characterize the time-dependent inflation of the magma source at Three Sisters.

To apply our two-step-approach (section 3.2), we use the median, and 5% and 95% percentile values of the PDF of depth estimated by the Bayesian inversion. The corresponding values are: $d_{median} = 5000\,m$, $d_{5\%} = 4500\,m$ and $d_{95\%} = 6000\,m$. The volume change time-series is determined using InSAR data from four satellite missions (ERS, ENVISAT, ALOS-1 and Sentinel-1), on five different tracks and look angles, and CGPS data from HUSB.

First, we obtain the increments of each volume change, ΔV_i, relating the Green's functions (representing the source impulse for a buried spherical point source) to the LOS deformation data observed along each satellite track and the three component CGPS data. Figures 6 and 7 respectively show results regarding estimation of the median value of source depth ($d_{median} = 5000\,m$) for InSAR and CGPS data. The cumulative increments of volume changes detected at HUSB show gaps due to ice and snow accumulation during winter. By means of the daily GPS measurements, the corresponding increments of volume change, ΔV_i, are more uniform for the CGPS data sets (Figure 7), but more variable for the individual SAR data sets (Figure 6).

Finally, we applied the Picard Plot condition suitable to understand the conditions of the ill-posed problem (Equation 3). Figure 8**A** shows how s_i only decays faster than the Fourier coefficients ($\left|u_i^T \Delta V_i\right|$) for the smallest nonzero singular values. Hence, the problem can be considered stable, discarding the last 10% of the singular values. Due to the stability of the problem, the Picard Plot provides no clues about the appropriate level of truncation (Equation 7). Therefore, we use L-curve to determine the truncation level. L-curve criterion is fulfilled when L-corner= 1198, i.e., when only the first 24.1% nonzero singular values are used in the inversion (Figure 8**B**).

The final inflation time-series is shown in Figure 10 and Table 4. The inflation time-series associated with the median estimation of the source depth suggests a maximum volume change rate of $\sim 1.60 \times 10^6\ {}^{m^3}/_{yr}$ during $1999 - 2001$ and a subsequent rate as much as $\sim 0.75 \times 10^6\ {}^{m^3}/_{yr}$ for the period 2015- January 2020. Data since 2018 show a subtle, but significant change in the trend, instead of following asymptotic behavior.

5 DISCUSSION

5.1 Source characterization

Studies at Three Sisters using InSAR interferometric pairs and stacks (Wicks, 2002; Riddick and Schmidt, 2011), GPS (campaign and continuous) and leveling (Dzurisin et al., 2009) assessed various source geometries such as spherical point, sill-like or crack and ellipsoidal. These different sources can all fit the data in a satisfactory way. Our results are consistent with previous findings (Table 3). However, volume change rates and depths vary slightly, possibly due to the fact that: (1) there may be a poorly resolved deeper magma sources, (2) inversions were limited to purely kinematic models, (3) the source not being a

simple model assuming an isotropic elastic half-space and/or not being stable, producing bias due to spatial or temporal considerations, (4) diverse inversion techniques and related possible mathematical artifacts, (5) different types of data sets and (6) ambiguity of source geometries. We assumed a simple, stable, purely kinematic model as a valid approach, following the results of Dzurisin et al. (2009) and Riddick and Schmidt (2011), for estimating volume time series. Now, we focus on discussing the implications of (4), (5) and (6).

A range of common techniques to estimate source location has been used, like forward modeling, grid search by iteratively fixing of one parameter, arithmetic mean to obtain range values, or grid search. However, the Bayesian approach presents important advantages: (1) robust inversion for a single or more InSAR interferograms with an acceptable signal-to noise-ratio and/or GPS data, (2) rapid simultaneous inversion of all model parameters; (3) use of data uncertainty and prior model information; and (4) efficient sampling of posterior PDFs to estimate optimal model parameters and the associated range of error. Bearing in mind such advantages, to obtain a robust estimate of source geometry and location we only need geodetic data with high spatial coverage, spanning the most appropriate period (shortest time, high deformation). For this, we use the period undergoing maximum deformation, displaying as much as $\sim 5\ cm$ of line-of-sight deformation (Figure 4). Selection of the ERS-1 track 365 (descending orbit) interferometric pair spanning August 1997- September 2000 satisfies both criteria. To reduce the signal-to-noise ratio, the interferogram is filtered for a pixel coherence threshold of 0.2. Other ERS-1 InSAR data were also processed for similar periods of time, but not used due to the low signal-to-noise ratio. No GPS data were available until 2001 and cannot be used to study the maximum uplift rate period.

The lack of a full 3D image of the deformation source, necessary to distinguish between different source geometries (Dieterich and Decker, 1975) and the almost symmetric shape of the 2D deformation pattern implies that source geometry is far from unique, and a wide range of sources are possible. We explore spherical point, prolate spheroid and sill-like sources providing similar misfit to the geodetic data. Although the sill location is well constrained, the size of the source was statistically poorly resolved. Radius and dimensionless excess pressure PDFs display a bi-modal shape (slightly unstable inversion results Figure 5). Similar bi-modality are found for PDFs of the prolate spheroid parameters.

Previous studies mentioned above revealed that the temporal evolution of the uplift signal can be represented by a time-invariant volcanic source geometry and location with a decreasing inflation rate. Therefore, we assume the source has not changed significantly either in shape nor in location since the onset of deformation. Furthermore, the misfit values does not significantly change when considering the sources to model different periods of the temporal series of inflation, obtaining similar estimations of the rate of volume change, even independently of source type. The differences between inversion methods and data selection might explain that our optimal inversion results suggest a slightly shallower source with a corresponding smaller increment of volume change. Despite that, considering that the models fit the data well and yield similar misfit values, we conclude that it is reasonable to assume the spherical point source as the simplest kinematic model that explains the signal. Furthermore, the values for depth and increments of volume change lie within our 95% credible intervals (Table 3). Wicks (2002) processed three interferograms, obtaining an increment of volume change of $\Delta V = 23 \times 10^6\ m^3$ and depth of 6500 m for the one with the largest apparent signal-to-noise ratio. Ultimately, a deeper source will trade-off with a greater ΔV, to fit the same surface deformation. Although the time acquisition of the best interferogram of Wicks (2002) spans only one year more than our InSAR data interferometric pair, the important difference between our $\Delta V_{rate} = \sim 3.00 \times 10^6\ {}^{m^3}/_{yr}$ and their $\Delta V_{rate} = \sim 5.75 \times 10^6\ {}^{m^3}/_{yr}$ is mainly due to their depth

estimation. Our InSAR interferogram matches one of the other two by Wicks (2002). For that interferogram, their model gives depths ~ 1 *km* shallower, being closer to our depth estimation.

5.2 Time series of volume changes: Regularization using the truncated SVD

To assess the effect of the regularization, we compared the increments of volume change (ΔV_i, Equation 1) and the corresponding simulated observations ($\Delta V_{i_{reconstruction}} = V_{(i+1)_{inversion}} - V_{i_{inversion}}$ from the results of Equation 6) for different levels of regularization. Figures 9**A** and 9**B** show the solution for an extreme regularization, using only the first 0.2% and 2% nonzero singular values (oversmoothing solutions). For the 0.2% case, the values of ΔV_i associated with the InSAR data display a wide dispersion, and the ΔV_i associated with GPS data acquire discrete values, i.e, the same ΔV_i value is obtained for many different time intervals. Figure 9**D** represents the case of non-regularization (less filtering, maximum solution size and minimum misfit). The residual in Figure 9**D** is minimized because the solution reproduces even the seasonal perturbations of the GPS data (undersmoothing solution). There is a seasonal deformation of the crust associated with the surface load of the snow cover. It is possible that the magma reservoir's internal pressure also fluctuates seasonally in response to this effect. However, from CGPS data alone we cannot resolve the cause of these fluctuations. Therefore, a smoother solution is preferred to depict the long-term deformation time series. This is given by the combination of Picard condition and L-curve criteria; it corresponds to the appropriate smoothing solution, i.e, 24.1% nonzero singular values (Figure 9**C**).

5.3 Time-scales of inter-eruptive uplift signals: Three Sisters and other volcanoes

The continuous and extended regularized time-series of volume change allow us to study the inflation process in detail. Riddick and Schmidt (2011) proposed a piece-wise linear parametrization with two changes in rate provides a good fit to uplift rates till 2009 explaining two different inflation processes beginning at 1998 and 2004 at Three Sisters. This model was supported by the detection of a seismic swarm in 2004. Our denser, longer time-series clearly show a smooth and continuous function, which we interpret as a fast inflation followed by relaxation of the crust (Figure 10). We are specifically interested on the interval of decaying rates. Consequently, the time-series is divided into two main intervals separating increasing and decaying behaviour of volume rates. An exponential function can reasonably reproduce the relaxation process. Therefore, we propose a piece-wise parametric of the form:

$$V(t) = \begin{cases} d & , t < t_0 \\ a - b\exp -(c \cdot (t - t_0)) & , t \geq t_0 \end{cases} \tag{8}$$

where a, b and d are constants, $1/c = \varepsilon$ is the characteristic relaxation time constant, here after named e-folding parameter, and t_0 is the start of the exponential trend. We solved the parameters of this model using a non-linear least-square fit. To minimize the influence of outliers, we used regression method: the Least Absolute Residuals (LAR) and Bisquare weights methods, considering also the data uncertainties (weighted). Four methods (Bisquare, Bisquare-Weighted, LAR, LAR-Weighted) show very similar fit, LAR performing the best (Figure 10, Table 4). Time-series from the median, and 5% and 95% percentiles

of the PDF distribution for depth, along with the variance of the curve fitting, permit constraining the lower and upper limits of e-folding and t_0 parameters.

Our time-series spans 26 years and presents a characteristic time constant of 9.48 $[+0.12, -0.17]$ years. This new result updates the value of 5.3 years obtained by Dzurisin et al. (2009) from an 8-year time-series of GPS displacements from 2001 to late 2008. Riddick and Schmidt (2011) hyphotesized that one injection of magma started between June 1996 and July 1997, given StaMPS results for T385 ERS. The updated volume time-series presented in this study shows a clear exponential decay trend. We estimate a start date for the exponential trend between October 1998 and August 1999 (Table 4). These results suggest that the continuous uplift signal will be detectable for a few decades, considering volume change rates as low as $0.1 \cdot 10^6\ m^3$. As late as January 2020, our inflation time-series indicated that the cumulative volume of a spherical point source with $d_{median} = 5000\ m$ is $29.1 \cdot 10^6\ m^3$. For $d_{5\%} = 4500\ m$ and $d_{95\%} = 6000\ m$, the values are $22.7 \cdot 10^6\ m^3$ and $39.9 \cdot 10^6\ m^3$, respectively. This range of values is consistent with those predicted by Dzurisin et al. (2009) for a prolate spheroid model, 44.9 to $51.6 \cdot 10^6 m^3$ (where the uncertainty is $10-20\%$ of those values). This estimation of the cumulative volume is 10 to 20 times less than the volume erupted from Mount St. Helens in May 1980 (Wicks, 2002).

To compare the characteristic relaxation time for other volcanoes with recent and well-studied unrest episodes, we compiled and modeled the available geodetic and volume time-series of the following volcanic systems: Okmok (Biggs et al., 2010, Figure 4), Long Valley (Hill et al., 2020, Figure 3a), Uturuncu (Lau et al., 2018, Figure 4), Laguna del Maule (Le Mével et al., 2015, Figure 2b), Yellowstone (Tizzani et al., 2015, Figure 2), Campi Flegrei (Troise et al., 2007, Figure 1b), Santorini (Parks et al., 2015, Figure 10), Alutu (Hutchison et al., 2016, Figure 7), Agung (Syahbana et al., 2019, Figure 3d). We estimated the e-folding parameter following equation (8), for $t > t_0$; i.e., comparing different volcanic systems, each with a different characteristic relaxation time. Greater e-folding indicates longer relaxation times, as shown in Figure 11**A**. The estimated e-folding parameters vary between 0.033 and 10 *years*, for uplift and inflation episodes lasting between 60 *days* and 26 *years*. Our selected volcanoes, particularly those of the North and South American volcanic arcs, present the longest e-folding times (Figure 11**B**).

From the small selection of volcanoes, neither the type nor composition of the volcanoes seems to be decisive for the characteristic relaxation time associated with their inter-eruptive periods. However, those with a shorter e-folding display significant changes in their behavior after relaxation. For instance, Campi Flegrei exhibited an increment in displacement from $1968-1972$, with an e-folding of 1.38 *years*. Next, the subsidence rate was small until 1982, and the deformation trend changed due to a new uplift episode during $1982-1983$, followed by subsidence during $1990-1995$. Those features were related to an overpressure in the magmatic source and fracturing of the rock volume between the magmatic fluids and the aquifer (Troise et al., 2007). Alutu underwent two inflation pulses, the latest showing a short e-folding or relaxation time of 0.033 *years*, during the period October-December 2008, then a slow deflation took place. These short time-scale suggest the migration of hydrothermal or magmatic fluids or volatiles (Hutchison et al., 2016). Agung went through an uplift from August-October 2017, characterized by an e-folding of 0.038 *years*, then in late November, a phreatomagmatic eruption and stronger explosions took place (Syahbana et al., 2019). Santorini presented a source inflation process with an e-folding of 0.28 *years* for the period October 2011- August 2012 (Parks et al., 2015). Then, its subsidence rates increased in the post-unrest period $2012-17$, suggesting the superimposition of various deformation sources (Papageorgiou et al., 2019). The Okmok inflation episode during the period May 2002 - September 2007 had an e-folding of 1.24 *years*. Although there was a small amount of deflation (Biggs et al., 2010), the general trend can be modeled as an exponential decay. After this inter-eruptive episode, a phreatomagmatic eruption occurred in

July–August 2008 (Larsen et al., 2015). Long Valley deformation series presents an e-folding of 5.31 *years* for the period $1978-1988$, with no significant seismicity detected during the interval $\sim 1986-1988$. After the exponential decaying trend, there was a renewed unrest, characterized by recurring earthquake swarms and tumescence of the resurgent dome (Hill et al., 2020). Yellowstone went through an uplift during $2005-2010$, with an estimated e-folding of 2.1 *years*. Since 2015, subsidence of Yellowstone caldera has occurred at an average rate of $2-3$ *cm* per year, as reported by Yellowstone Volcano Observatory (USGS). Laguna del Maule is the only volcano that yields a high relaxation time value for a short inter-eruptive period ($2010-14$), according to Le Mével et al. (2015). However, the fit of the data for this period could also be due to a linear inflation pulse superimposed on an exponentially decaying deformation rate. On the other hand, Uturuncu and Three Sisters present the longest e-folding (8.93 *years* and 9.48 *years*), without showing significant changes in their volcanic activity. Although these results are very preliminary and statistically unimportant, the e-folding parameter seems to be an informative variable in the magnitude of the inter-eruptive period time scales and its relationship with the restart of unrest in these particular volcanic systems.

We re-scaled the observed time-series to properly emphasize similarities on the exponential decay. We normalize displacement or volume change (y'), as a function of normalized time by means of the e-folding parameter (t'):

$$y'(t) = (y(t) - y_0)/(y_{t_\infty} - y_0) \tag{9}$$

$$t' = (t - t_0)/\varepsilon \tag{10}$$

where y_0 is the displacement or volume change at t_0, y_{t_∞} is the value after total relaxation (i.e, at $t = t_\infty$), and t_0 is the onset of the exponential function. It is worth noting that using the e-folding parameter accurately represent the characteristic relaxation times, and hence re-scales invariantly the observations.

Figures 11**C**, **D** and **E** show the resulting normalized time-series for each volcano, revealing a strikingly similar pattern. This behavior seems to be independent of the e-folding value or duration of the inter-eruptive episode. Accordingly, the temporal invariance could indicate that there is a limited set of physical scenarios underlying inter-eruptive inflation episodes. This evidence rules out inter-eruptive physical processes other than those with an exponential time-dependent solution. Several physical models could explain deformation with this pattern (e.g., Lengliné et al., 2008, Reverso et al., 2014, Walwer et al., 2019). Dzurisin et al. (2009) put forward several mechanistic explanations for Three Sisters: (1) hydraulic pressurization or instantaneous response of the crust to continued intrusion at depth; (2) pressurization of the hydrothermal system; (3) viscoelastic response of the crust due to an intrusion emplaced at depth. Zurek et al. (2012) concluded, based on the lack of gravity change from 2002-2009, that deformation at Three Sisters reflects a viscoelastic response of the crust to a previous intrusion of magma. Our analyses, which localized the start of the exponential decay around 1998-1999, favors the hypothesis of a viscoelastic response of the crust. Future work should be focused on whether the deformation could be a viscoelastic response to a very rapid magma emplacement or to several years of active intrusion of magma. Although limited in scope, this analysis is a step towards understanding the time-scale of inter-eruptive processes. In regards to eruption forecasting, the uplift/inflation itself cannot be used as a pre-eruptive precursor without knowing what controls it through the combination of petrological and/or geophysical data.

6 CONCLUSION

The evolution of volume change time-series at active volcanoes can be studied by combining heterogeneous geodetic datasets. For Three Sisters volcano, we combined high spatial coverage from multiple InSAR satellite data and long term temporal information on the three-components of the only available continuous GPS. We improved a previous two-step approach to volume time-series reconstruction, by including a non-arbitrary truncation level. The cut-off criterion for truncation (i.e., type of filter) is necessary to obtain a solution without too much loss of resolution affecting the stability of the inversion. We proposed a method that combines the Discrete Picard Condition and the L-curve. Furthermore, our approach takes propagation errors into account in all inversion steps. The final time-series is determined considering volume change rates instead of increments of displacement, avoiding problems deriving from the amplification of uncorrelated noise between adjacent GPS data or propagation through the time-series of the uncertainty of the first acquisition.

The inflation time-series of Three Sisters since 2018 shows a noticeable change in the trend, which departs from the previous asymptotic trend towards a constant decay rate. This change can be explained by a fixed step in the position, such as that caused by a change in the instrumentation or monumentation. However, we cannot rule out a minor injection of magma or fluid pressurization beneath Three Sisters. Considering the wide range of erupted magma compositions and eruption styles, any changes in the Three Sisters background uplift behavior should be evaluated as an important indicator of future volcanic activity.

The Three Sisters volcano uplift is still on-going. The Bayesian inversion of source parameters gives 95% credible intervals, the depth for a spherical point source being between $(4500 - 6000)$ m. Parametric modeling of the inflation time-series associated with the median, and 5% and 95% percentiles of source depth allow us to constrain the onset of the exponential trend to between October 1998 and August 1999 and the characteristic relaxation time to 9.48 $[+0.12, -0.17]$ years. Therefore, in the absence of different or new unrest signals, we estimate a continuous uplift signal, at diminishing but detectable rates, lasting for few decades (currently estimate to 2054$[\pm 2$ years$]$).

Inter-eruptive uplift/volume change signals of analyzed volcanoes show rather simple and time-scale invariant behaviour, after a proper scaling. We interpret this observation as pointing to a rather reduced set of physical mechanisms underlying inter-eruptive inflation episodes that are consistent with exponential decay (viscoelastic response and/or hydraulic pressurization). Furthermore, we suggest that the magnitude of the characteristic relaxation time can be indicative of significant changes of background behaviour on volcanoes. Temporally persistent, long-lasting and overlapping uplift signals are potential confounding indicators for the classic inflation-eruption-deflation cycle model. We highlight the importance of high-temporal and continuous surface deformation monitoring to identify any departures of background temporal behaviour (potentially very complex), as an indicator of future eruption hazard in persistent uplifting volcanoes.

CONFLICT OF INTEREST STATEMENT

The authors declare that the research was conducted in the absence of any commercial or financial relationships that could be construed as a potential conflict of interest.

AUTHOR CONTRIBUTIONS

SRM processed radar images, performed modelling, carried out the comparison among different volcanic systems, prepared the figures and co-wrote the manuscript. PJG and DS processed radar images. MC and PJG conceptualized the study, interpreted results and co-wrote the manuscript. ANM co-supervised SRM and contributed to the manuscript. DS contributed to the manuscript.

FUNDING

Part of this work was carried out during research visits of SRM to the University of Liverpool and the U.S. Geological Survey (USGS) Cascades Volcano Observatory (CVO). PJG was supported by the United Kingdom NERC project Centre for the Observation and Modelling of Earthquakes, Volcanoes and Tectonics (COMET, GA/13/M/031, comet.nerc.ac.uk). SRM, MC and AMN research was supported by MINECO project CGL2014-58821-C2-1-R. SRM was also supported by MINECO fellowship BES-2015-074228.

ACKNOWLEDGMENTS

We would like to thank Mike Lisowsky for providing the predicted horizontal tectonic motion at HUSB.We would like to thank Yu Jiang for his support in InSAR processing and Xiao Wang for his help with the University of Liverpool, School of Environmental Sciences computing resources. This manuscript was edited by Guido Jones, currently funded by the Cabildo de Tenerife, under the TFinnova Programme supported by MEDI and FDCAN funds. We also acknowledge M. Battaglia and anonymous reviewer their thoughtful comments and suggestions.

DATA AVAILABILITY STATEMENT

JAXA/METI ALOS PALSAR L1.0 was accessed through ASF DAAC, https://asf.alaska.edu [June 2018] doi:10.5067/J4JVCFDDPEW1. ERS-1, ESA [1997-2000] downloaded from ASF DAAC, https://asf.alaska.edu [June 2018]. Copernicus Sentinel data was retrieved from ASF DAAC, https://asf.alaska.edu [June 2018]. This work contains modified Copernicus Sentinel data [2014-2018], processed by ESA. HUSB CGPS data and errors were obtained from the Pacific Northwest network on the USGS website https://earthquake.usgs.gov/monitoring/gps/Pacific_Northwest/husb.

REFERENCES

Backus, G. E. (1988). Bayesian inference in geomagnetism. *Geophysical Journal International* 92, 125–142. doi:10.1111/j.1365-246X.1988.tb01127.x

548 Bagnardi, M. and Hooper, A. (2018). Inversion of Surface Deformation Data for Rapid Estimates of
549 Source Parameters and Uncertainties: A Bayesian Approach. *Geochemistry, Geophysics, Geosystems* 19,
550 2194–2211. doi:10.1029/2018GC007585
551 Battaglia, M., Cervelli, P., and Murray, J. (2013). Dmodels: A matlab software package for modeling
552 crustal deformation near active faults and volcanic centers. *Journal of Volcanology and Geothermal*
553 *Research* 254, 1–4. doi:10.1016/j.jvolgeores.2012.12.018
554 Bekaert, D. P. S., Hamlington, B. D., Buzzanga, B., and Jones, C. E. (2017). Spaceborne synthetic
555 aperture radar survey of subsidence in hampton roads, virginia (usa). *Scientific Reports* doi:10.1038/
556 s41598-017-15309-5
557 Berardino, P., Fornaro, G., Lanari, R., and Sansosti, E. (2002). A new algorithm for monitoring localized
558 deformation phenomena based on small baseline differential SAR interferograms. *IEEE International*
559 *Geoscience and Remote Sensing Symposium* 2, 2375–2383. doi:10.1109/IGARSS.2002.1025900
560 Biggs, J., Lu, Z., Fournier, T., and Freymueller, J. T. (2010). Magma flux at Okmok Volcano, Alaska,
561 from a joint inversion of continuous GPS, campaign GPS, and interferometric synthetic aperture radar.
562 *Journal of Geophysical Research: Solid Earth* 115, 1–11. doi:10.1029/2010JB007577
563 Biggs, J. and Pritchard, M. (2017). Global volcano monitoring: What does it mean when volcanoes deform?
564 *Elements* 13, 17–22. doi:10.2113/gselements.13.1.17
565 Chen, C. W. and Zebker, H. A. (2002). Phase unwrapping for large sar interferograms: statistical
566 segmentation and generalized network models. *IEEE Transactions on Geoscience and Remote Sensing*
567 40, 1709–1719
568 Decriem, J., Árnadóttir, T., Hooper, A., Geirsson, H., Sigmundsson, F., Keiding, M., et al. (2010). The
569 2008 may 29 earthquake doublet in sw iceland. *Geophysical Journal International - GEOPHYS J INT*
570 181, 1128–1146. doi:10.1111/j.1365-246X.2010.04565.x
571 Dieterich, J. H. and Decker, R. W. (1975). Finite element modeling of surface deformation associated
572 with volcanism. *Journal of Geophysical Research (1896-1977)* 80, 4094–4102. doi:10.1029/
573 JB080i029p04094
574 Dzurisin, D., Lisowski, M., and Wicks, C. W. (2009). Continuing inflation at Three Sisters volcanic
575 center, central Oregon Cascade Range, USA, from GPS, leveling, and InSAR observations. *Bulletin of*
576 *Volcanology* 71, 1091–1110. doi:10.1007/s00445-009-0296-4
577 Dzurisin, D., Lisowski, M., Wicks, C. W., Poland, M. P., and Endo, E. T. (2006). Geodetic observations and
578 modeling of magmatic inflation at the Three Sisters volcanic center, central Oregon Cascade Range, USA.
579 *Journal of Volcanology and Geothermal Research* 150, 35–54. doi:10.1016/j.jvolgeores.2005.07.011
580 Farr, T. G., Rosen, P. A., Caro, E., Crippen, R., Duren, R., Hensley, S., et al. (2007). The shuttle radar
581 topography mission. *Reviews of Geophysics* 45. doi:10.1029/2005RG000183
582 Fialko, Y., Khazan, Y., and Simons, M. (2001). Deformation due to a pressurized horizontal circular crack
583 in an elastic half-space, with applications to volcano geodesy. *Geophysical Journal International* 146(1),
584 181–19
585 González, P. J., Samsonov, S. V., Pepe, S., Tiampo, K. F., Tizzani, P., Casu, F., et al. (2013). Magma storage
586 and migration associated with the 2011-2012 El Hierro eruption: Implications for crustal magmatic
587 systems at oceanic island volcanoes. *Journal of Geophysical Research: Solid Earth* 118, 4361–4377.
588 doi:10.1002/jgrb.50289
589 Hansen, P. C. (1990). The discrete picard condition for discrete ill-posed problems. *Bit* 30, 658–672.
590 doi:10.1007/BF01933214
591 Hansen, P. C. (1992). Analysis of Discrete Ill-Posed Problems by Means of the L-Curve. *SIAM Review* 34,
592 561–580. doi:10.1137/1034115

Hansen, P. C. (2007). Regularization Tools version 4.0 for Matlab 7.3. *Numerical Algorithms* 46, 189–194. doi:10.1007/s11075-007-9136-9

Hansen, P. C. and O'Leary, D. P. (1993). The Use of the L-Curve in the Regularization of Discrete Ill-Posed Problems. *SIAM Journal on Scientific Computing* 14, 1487–1503. doi:10.1137/0914086

Hill, D., Montgomery-Brown, E., Shelly, D., Flinders, A., and Prejean, S. (2020). Post-1978 tumescence at long valley caldera, california: A geophysical perspective. *Journal of Volcanology and Geothermal Research* 400, 106900. doi:10.1016/j.jvolgeores.2020.106900

Hooper, A., Bekaert, D., Spaans, K., and Arikan, M. (2012). Recent advances in SAR interferometry time series analysis for measuring crustal deformation. *Tectonophysics* 514-517, 1–13. doi:10.1016/j.tecto.2011.10.013

Hossainali, M., Becker, M., and Groten, E. (2010). Comprhensive Approach to the Analysis of the 3D Kinematics Deformation with appliction to the Kenai Peninsula. *Journal of Geodetic Science* 1. doi:10.2478/v10156-010-0008-1

Hutchison, W., Biggs, J., Mather, T. A., Pyle, D. M., Lewi, E., Yirgu, G., et al. (2016). Causes of unrest at silicic calderas in the east african rift: New constraints from insar and soil-gas chemistry at aluto volcano, ethiopia. *Geochemistry, Geophysics, Geosystems* 17, 3008–3030. doi:10.1002/2016GC006395

Larsen, J., Neal, C., Schaefer, J., Kaufman, A., and Lu, Z. (2015). *The 2008 phreatomagmatIc eruption of Okmok volcano, AleutIan Islands, Alaska: Chronology, deposits, and landform changes*. Tech. rep., State of Alaska, Department of Natural Resources, Division of Geological & Geophysical Surveys

Lau, N., Tymofyeyeva, E., and Fialko, Y. (2018). Variations in the long-term uplift rate due to the altiplano–puna magma body observed with sentinel-1 interferometry. *Earth and Planetary Science Letters* 491, 43–47. doi:10.1016/j.epsl.2018.03.026

Lawless, J. and Wang, P. (1976). A simulation study of ridge and other regression estimators. *Commun. Statist. Theor. Meth., A5, 307-323.*

Le Mével, H., Feigl, K. L., Córdova, L., DeMets, C., and Lundgren, P. (2015). Evolution of unrest at laguna del maule volcanic field (chile) from insar and gps measurements, 2003 to 2014. *Geophysical Research Letters* 42, 6590–6598. doi:10.1002/2015GL064665

Lengliné, O., Marsan, D., Got, J.-L., Pinel, V., Ferrazzini, V., and Okubo, P. G. (2008). Seismicity and deformation induced by magma accumulation at three basaltic volcanoes. *Journal of Geophysical Research: Solid Earth* 113. doi:10.1029/2008JB005937

Lohman, R. B. and Simons, M. (2005). Some thoughts on the use of InSAR data to constrain models of surface deformation: Noise structure and data downsampling doi:10.1029/2004GC000841

Menke, W. (1989). *Geophysiocal Data Analysis: Discrete Inverse Theory* (Academic, San Diego, Calif.)

Mogi, K. (1958). Relations between the eruptions of various volcanoes and the deformations of the ground surfaces around them. *Bull. Earthquake Res. Inst. Univ. Tokyo* 36, 99–134

Papageorgiou, E., Foumelis, M., Trasatti, E., Guido, V., Raucoules, D., and Mouratidis, A. (2019). Multi-sensor sar geodetic imaging and modelling of santorini volcano post-unrest response. *Remote Sensing* 11. doi:10.3390/rs11030259

Parks, M., Moore, J., Papanikolaou, X., Biggs, J., Mather, T., Pyle, D., et al. (2015). From quiescence to unrest: 20years of satellite geodetic measurements at santorini volcano, greece. *Journal of Geophysical Research B: Solid Earth* 120. doi:10.1002/2014JB011540

Poland, M. P., Lisowski, M., Dzurisin, D., Kramer, R., McLay, M., and Pauk, B. (2017). Volcano geodesy in the Cascade arc, USA. *Bulletin of Volcanology* 79. doi:10.1007/s00445-017-1140-x

Reverso, T., Vandemeulebrouck, J., Jouanne, F., Pinel, V., Villemin, T., Sturkell, E., et al. (2014). A two-magma chamber model as a source of deformation at grímsvötn volcano, iceland. *Journal of*

Geophysical Research: Solid Earth doi:10.1002/2013JB010569

Riddick, S. N. and Schmidt, D. A. (2011). Time-dependent changes in volcanic inflation rate near Three Sisters, Oregon, revealed by InSAR. *Geochemistry, Geophysics, Geosystems* 12, 1–14. doi:10.1029/2011GC003826

Rosen, P., Henley, S., Peltzer, G., and Simons, M. (2004). Updated repeat orbit interferometry package released. *Eos, Transactions American Geophysical Union* 85. doi:10.1029/2004EO050004

Rosen, P. A., Gurrola, E., Sacco, G. F., and Zebker, H. (2012). The insar scientific computing environment. In *EUSAR 2012; 9th European Conference on Synthetic Aperture Radar*. 730–733

Syahbana, D., Kasbani, K., Suantika, G., Prambada, O., Andreas, A., Saing, U., et al. (2019). The 2017–19 activity at mount agung in bali (indonesia): Intense unrest, monitoring, crisis response, evacuation, and eruption. *Scientific Reports* 9. doi:10.1038/s41598-019-45295-9

Tikhonov, A. and Arsenin, V. (1977). *Solutions of Ill-posed Problem* (John Wiley & Sons, New York.)

Tizzani, P., Castaldo, R., Pepe, A., Zeni, G., Lanari, R., and Battaglia, M. (2015). Magma and fluid migration at yellowstone caldera in the last three decades inferred from insar, leveling and gravity measurements. *Journal of Geophysical Research: Solid Earth* 120. doi:10.1002/2014JB011502

Troise, C., De Natale, G., Pingue, F., Obrizzo, F., De Martino, P., Tammaro, U., et al. (2007). Renewed ground uplift at campi flegrei caldera (italy): New insight on magmatic processes and forecast. *Geophysical Research Letters* 34, –L03301+. doi:10.1029/2006GL028545

Walwer, D., Ghil, M., and Calais, E. (2019). Oscillatory nature of the okmok volcano's deformation. *Earth and Planetary Science Letters* 506, 76 – 86. doi:https://doi.org/10.1016/j.epsl.2018.10.033

Weiss, J., Walters, R., Morishita, Y., Wright, T., Lazecky, M., Wang, H., et al. (2020). High-resolution surface velocities and strain for Anatolia from Sentinel-1 InSAR and GNSS data. *Geophysical Research Letters* doi:10.1029/2020GL087376

Wicks, C. W. (2002). Magmatic activity beneath the quiescent Three Sisters volcanic center, central Oregon Cascade Range, USA. *Geophysical Research Letters* 29, 2–5. doi:10.1029/2001GL014205

Yang, X.-M., Davis, P. M., and Dieterich, J. H. (1988). Deformation from inflation of a dipping finite prolate spheroid in an elastic half-space as a model for volcanic stressing. *Journal of Geophysical Research: Solid Earth* 93, 4249–4257. doi:10.1029/JB093iB05p04249

Zurek, J., Williams-Jones, G., Johnson, D., and Eggers, A. (2012). Constraining volcanic inflation at three sisters volcanic field in oregon, usa, through microgravity and deformation modeling. *Geochemistry, Geophysics, Geosystems* 13, 10013–. doi:10.1029/2012GC004341

FIGURE CAPTIONS

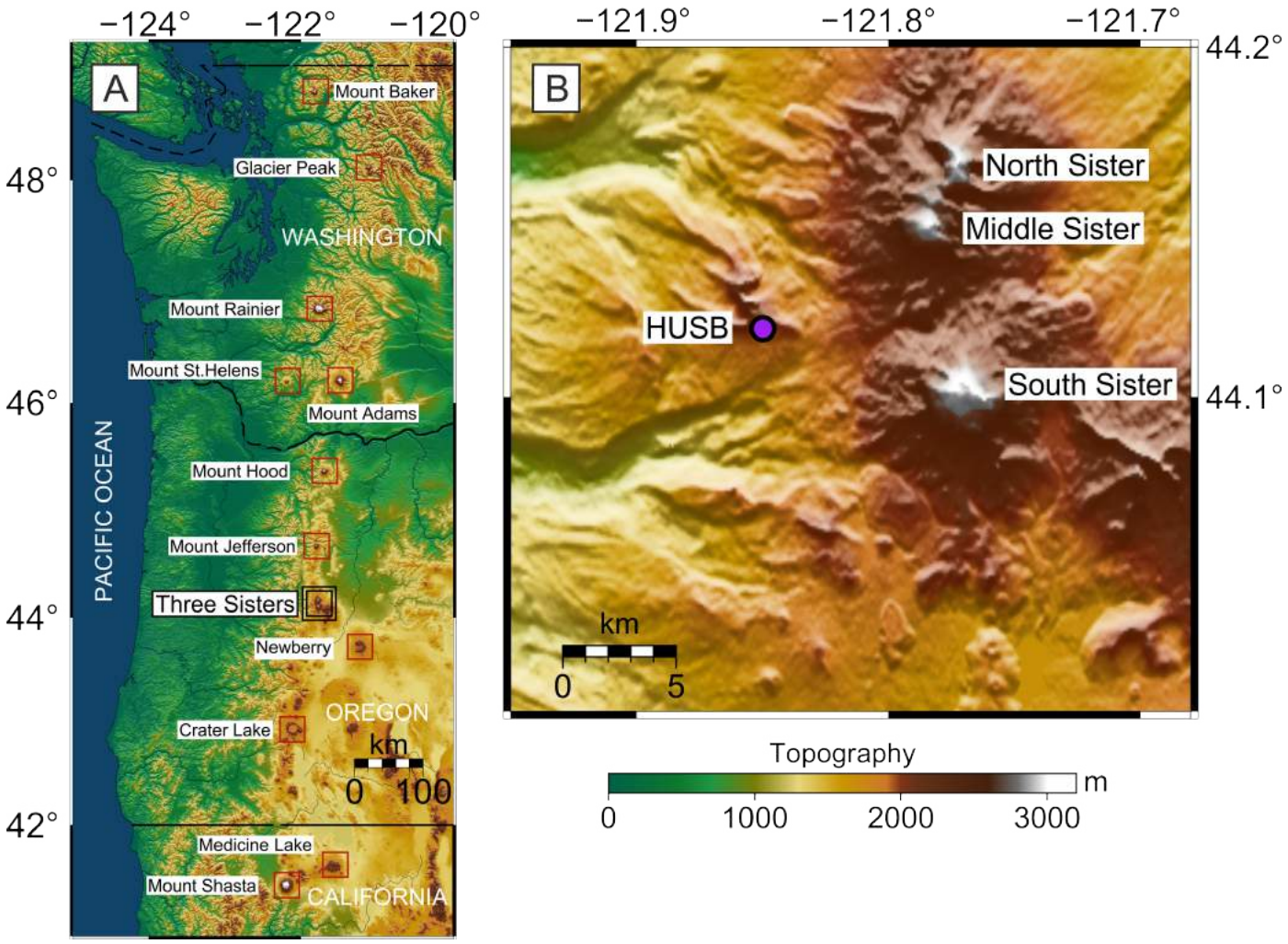

Figure 1. **(A)**: Shaded relief map for the Cascade range, with locations of representative Cascade volcanoes. Three sisters volcano is highlighted with black squares. **(B)**: Regional map of Three Sisters volcano complex. The continuous GPS station HUSB, located at $\sim$ 5 *km* west of South Sister volcano, is shown as a purple circle with black outline.

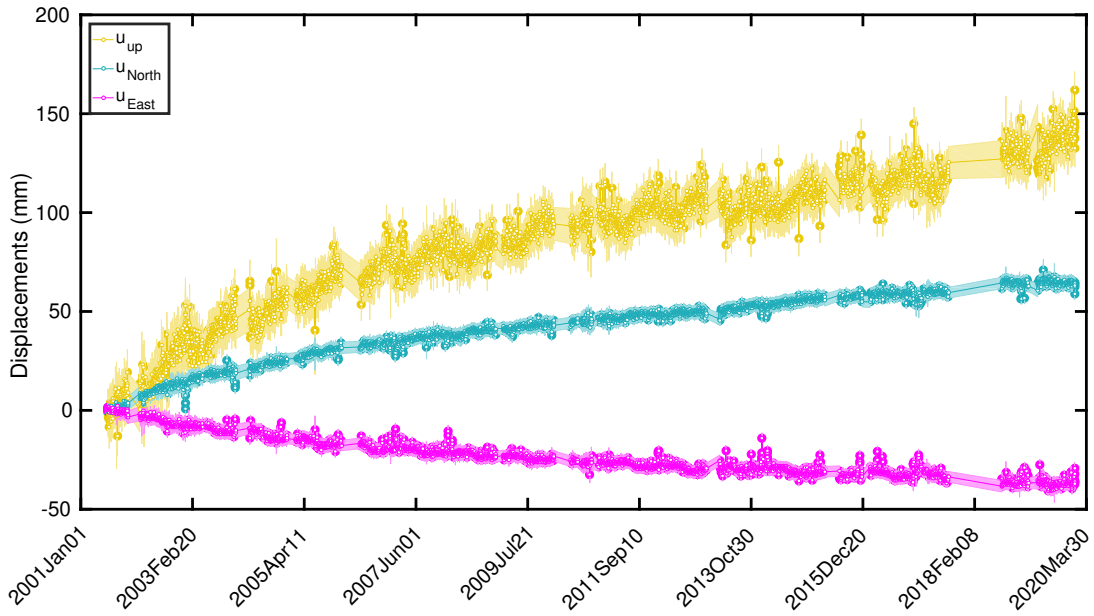

Figure 2. North (U_{North}), east (U_{East}) and vertical (U_{up}) components of the continuous GPS displacements at HUSB.

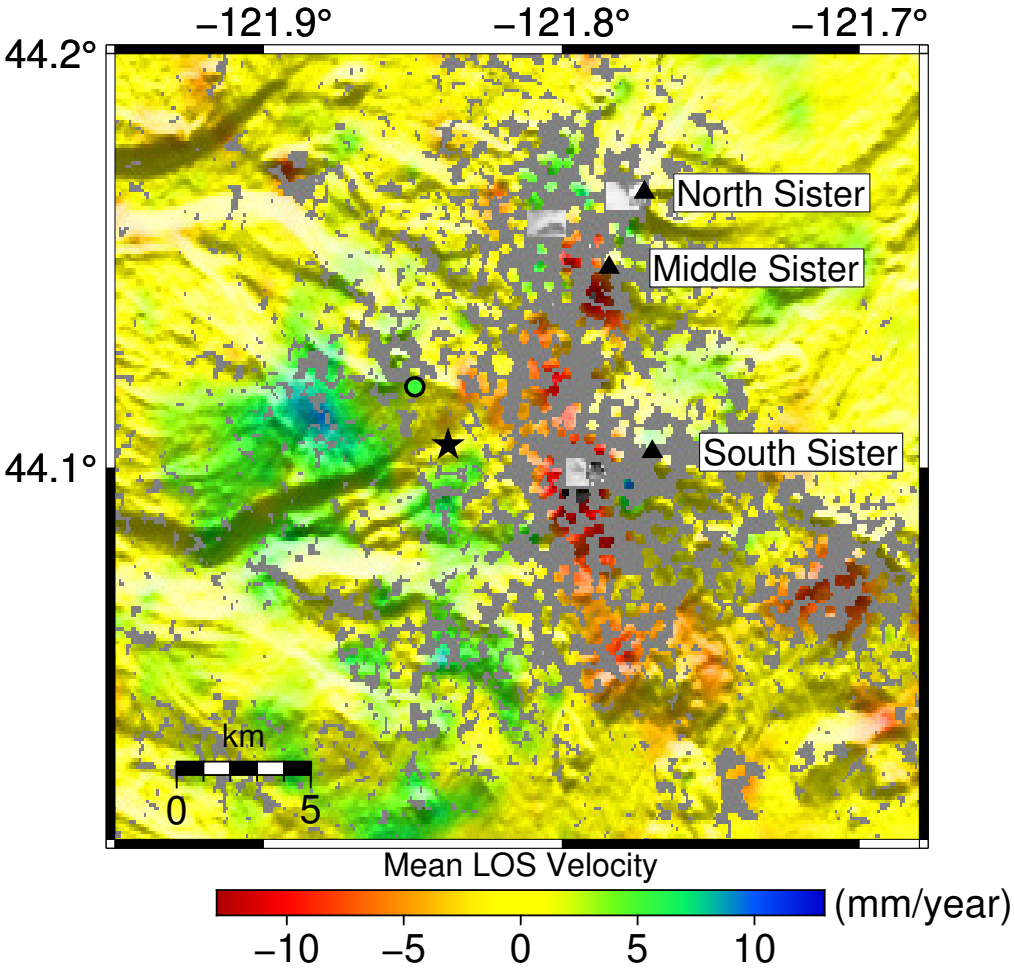

Figure 3. The linear surface deformation LOS velocity ($mm/year$) obtained for the ascending Path 219 ALOS-1, using the small baselines method implemented in StaMPS (Hooper et al., 2012) for the period January 2007 to March 2011. Positive LOS velocity values corresponds to displacements towards the satellite, i.e., uplifting. Black triangles and star represent the Three Sister complex volcano system and the approximate center of the uplifting area. StaMPS LOS velocity results were noisy and we post-processed to reduce undesirable oscillations of non-volcanic origin. We applied a band pass filter to retain spatial deformation signals between 10 and 0.8 km using a median filter (GMT blockmedian). Results indicate a 6 km circular uplift pattern west of South Sister with a mean LOS velocity of approximately $5-10$ $mm/year$, consistent with a value obtained for the Husband CGPS station during the same period (5.21 $mm/year$), shown as circle with a black outline.

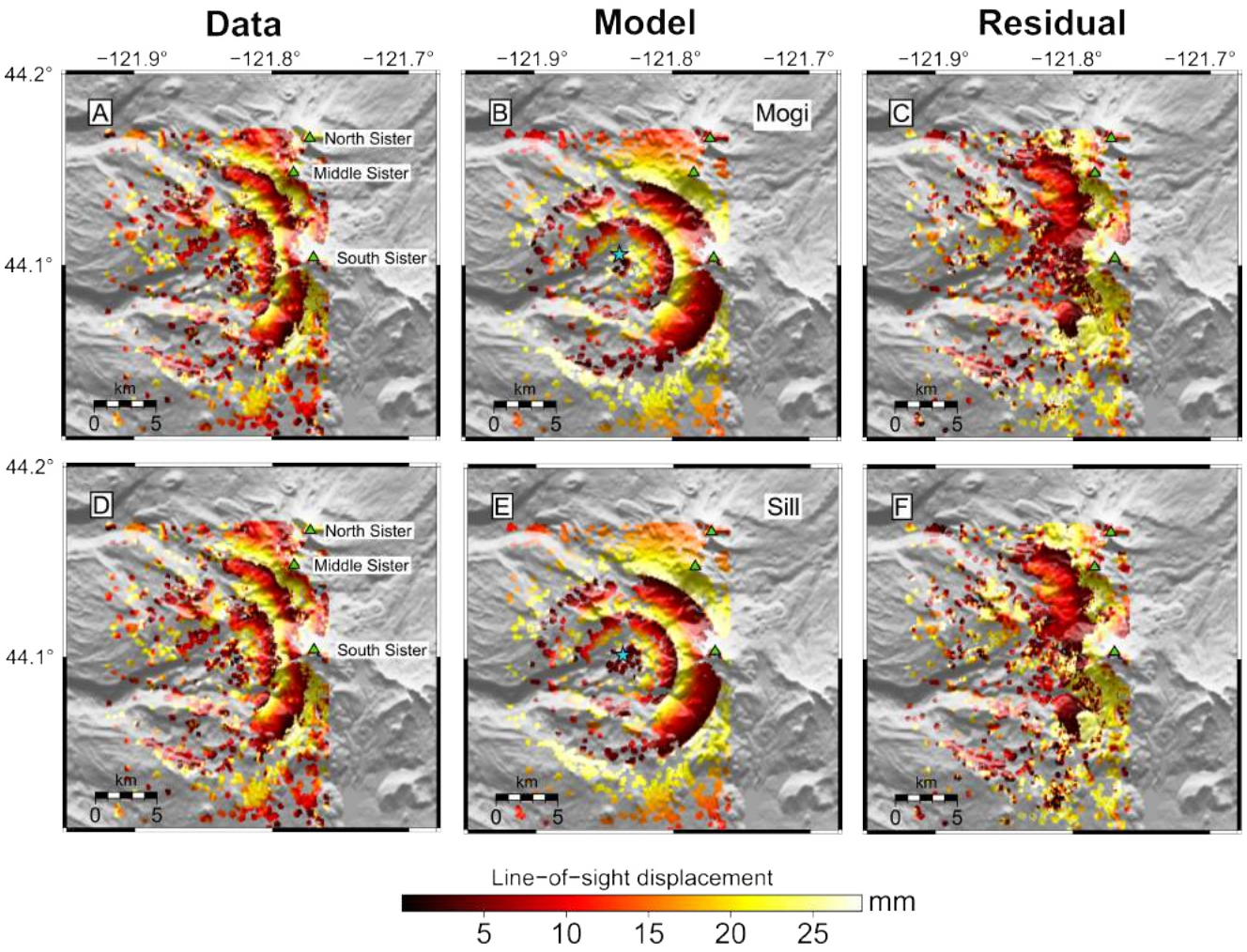

Figure 4. Wrapped InSAR data and model results for Track 385 of the ERS satellite. **(A)**, **(D)**: Line-of-sight (LOS) deformation observed in a nearly 3 years period from 24 August 1997 and 17 September 2000, considering only pixels with coherence$>$ 0.2. Green triangles represent the Three Sister complex volcano system. **(B)**, **(E)**: Bayesian model and horizontal location for the median a posteriori probability solution (blue star) for a predicted Mogi and sill-like source, respectively. **(C)**, **(F)**: Residual maps for Mogi and sill-like source. The model parameters results are presented in Figure 5 and Tables 1 and 2.

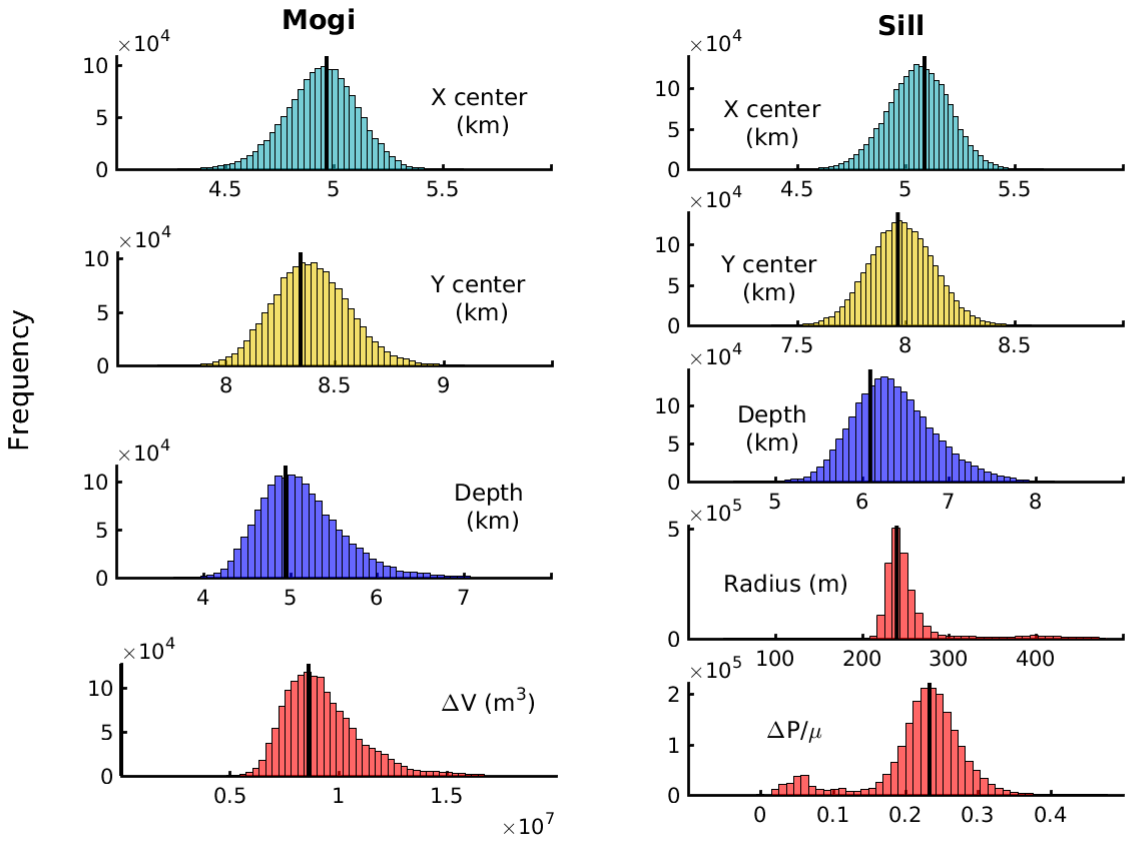

Figure 5. Posterior probability distributions for the Mogi and sill-like source models. Black solid lines show the optimal value for the corresponding model parameter (Table 1 and 2).

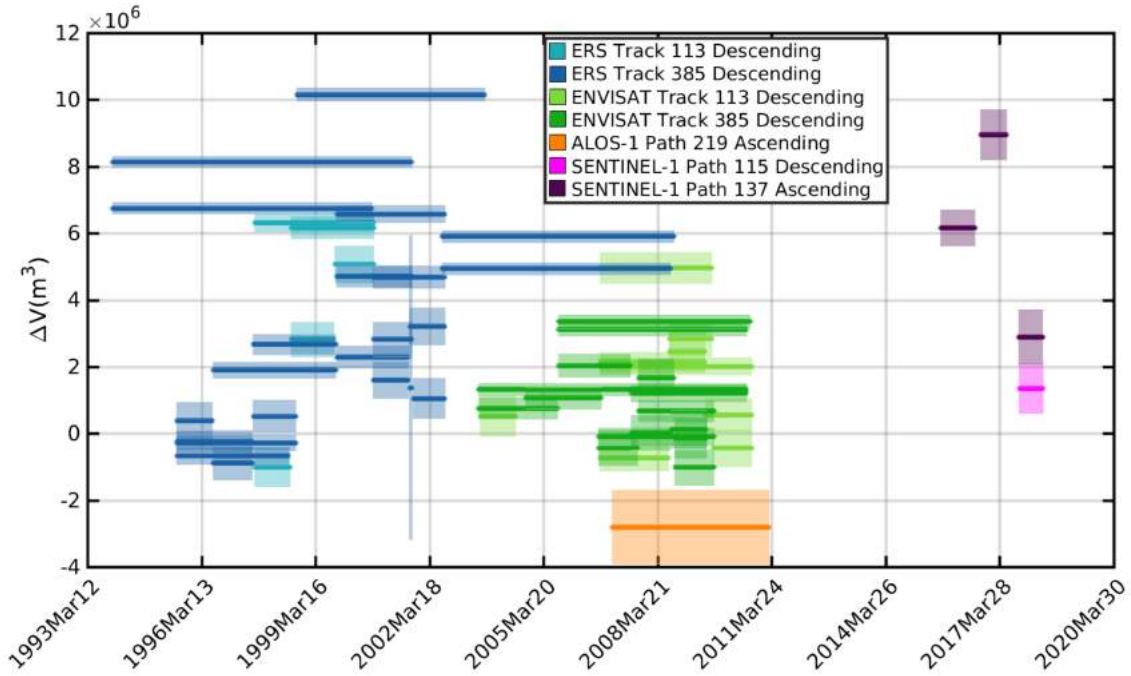

Figure 6. Increments of volume change obtained for all interferograms (ERS, ENVISAT, ALOS-1 and SENTINEL-1), according with the median value for the source depth.

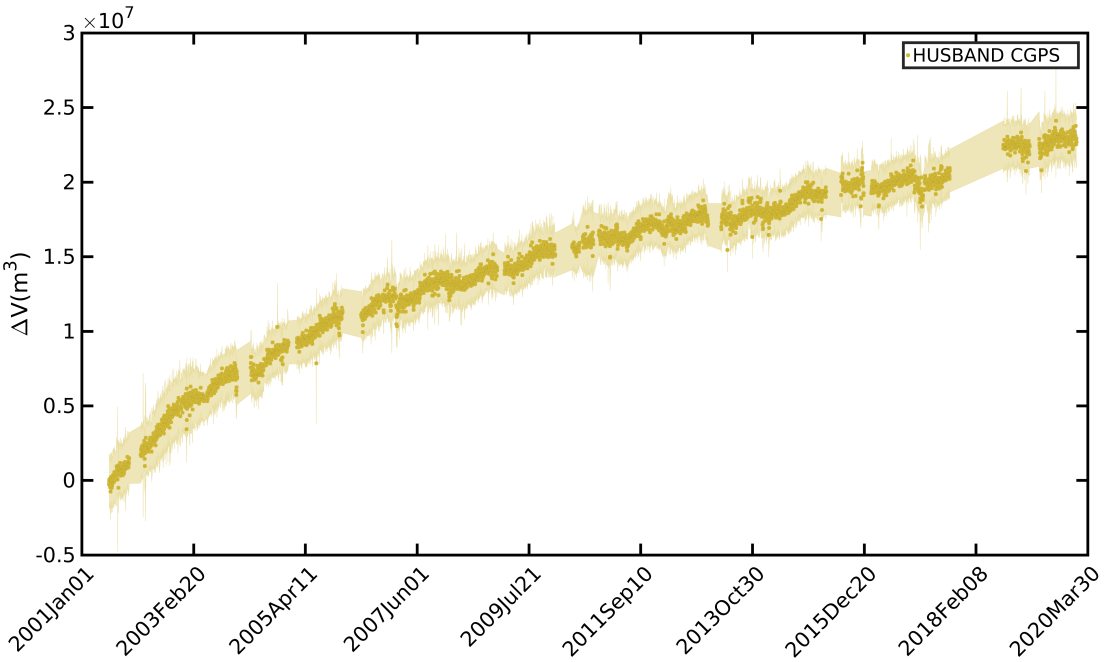

Figure 7. Cumulative increments of volume changes for the CGPS station, Husband. The figure shows the results according with the median value for the source depth.

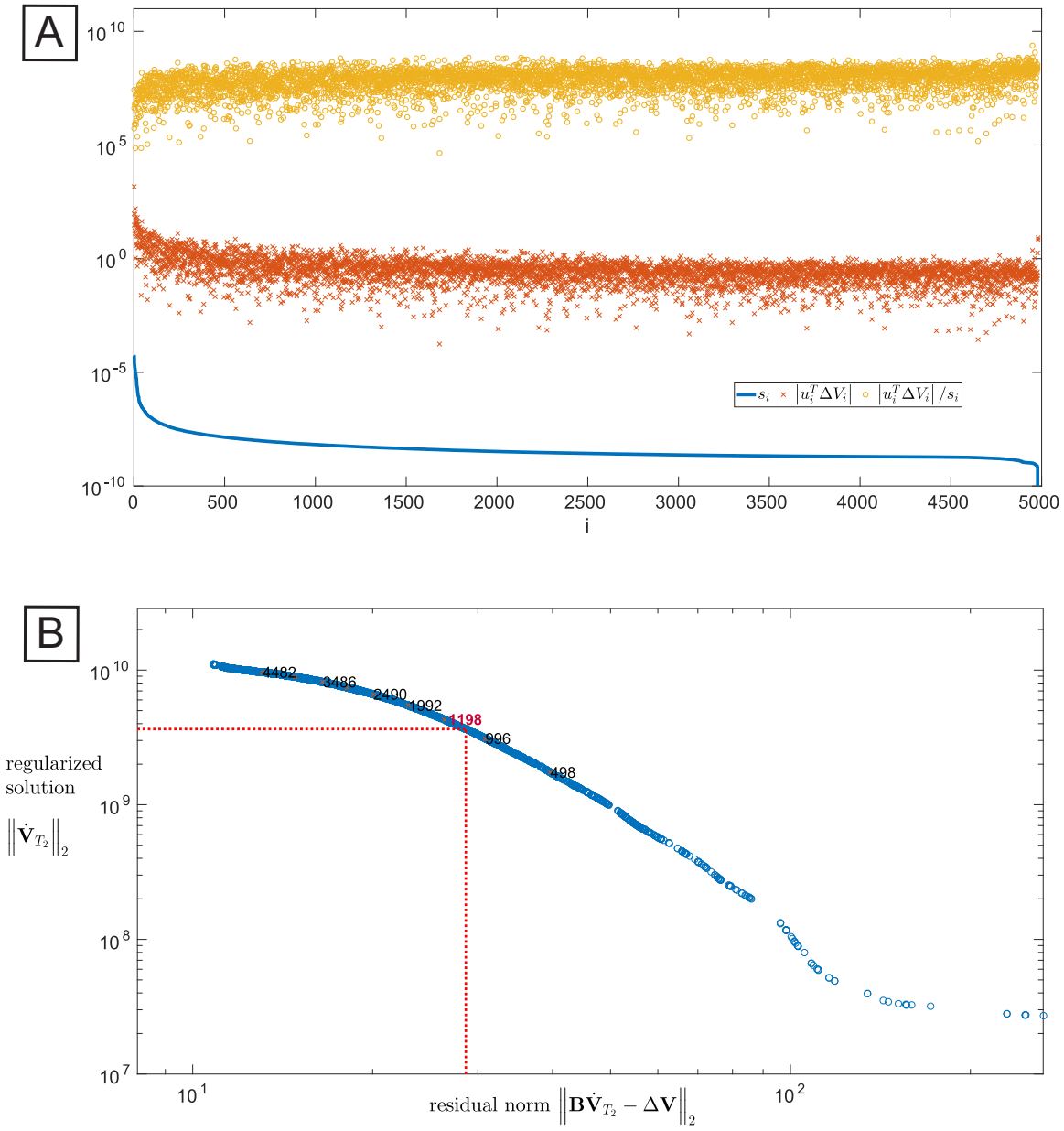

Figure 8. **(A)**: Discrete Picard Plot condition, suited for the analysis of ill-posed problems. The solution is stable when the Fourier coefficients, $\left|u_i^T \Delta V_i\right|$, on average decay to zero faster than the reciprocal singular values, s_i. In this case, the problem can be consider stable, discarding the last 10% singular values. **(B)**: L-curve showing the trade-off between minimizing the residual norm ($\left\|\mathbf{B}\dot{\mathbf{V}}_{T_2} - \Delta\mathbf{V}\right\|_2$) and minimizing the regularized solution size ($\left\|\dot{\mathbf{V}}_{T_2}\right\|_2$). The L-corner (represented in red) is located exactly where the solution changes in nature from oversmoothing (i.e, dominated by regularization errors) to being dominated by residual size.

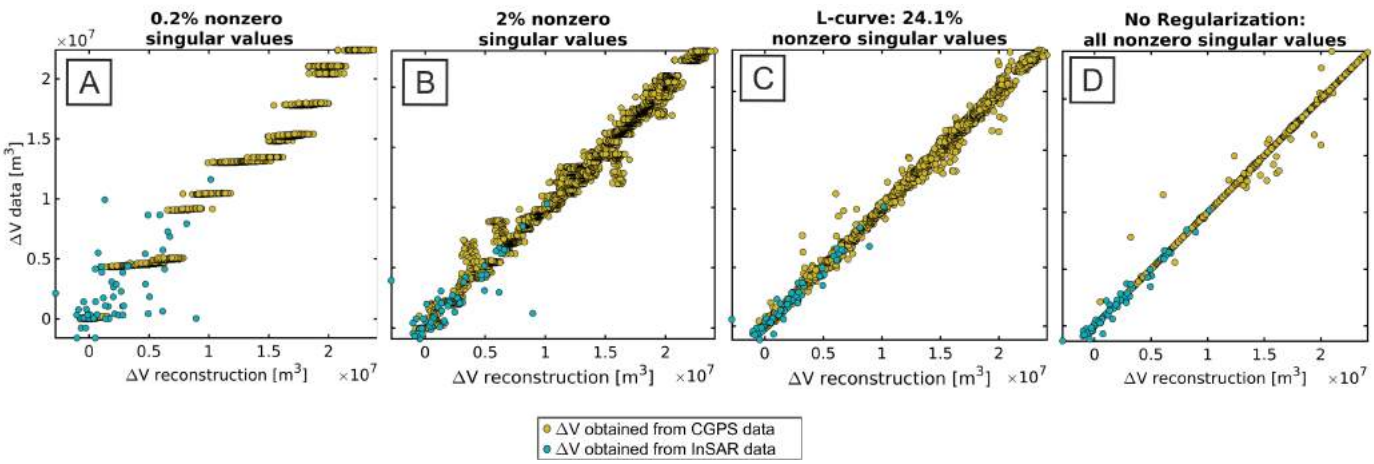

Figure 9. ΔV_i data (increment of volume change obtained from InSAR and CGPS deformation data, Equation 1), versus Simulated observations ($\Delta V_{i_{reconstruction}} = V_{(i+1)} - V_i$, Equation 6). **(A)** and **(B)**: Inversion solutions with regularization, using only the first 0.2% and 2% nonzero singular values, respectively (oversmoothing solution). **(C)**: regularized solution using the L-curve criteria corresponding with 24.1% nonzero singular values (appropriate smoothing solution). **(D)**: no regularization case (undersmoothing solution).

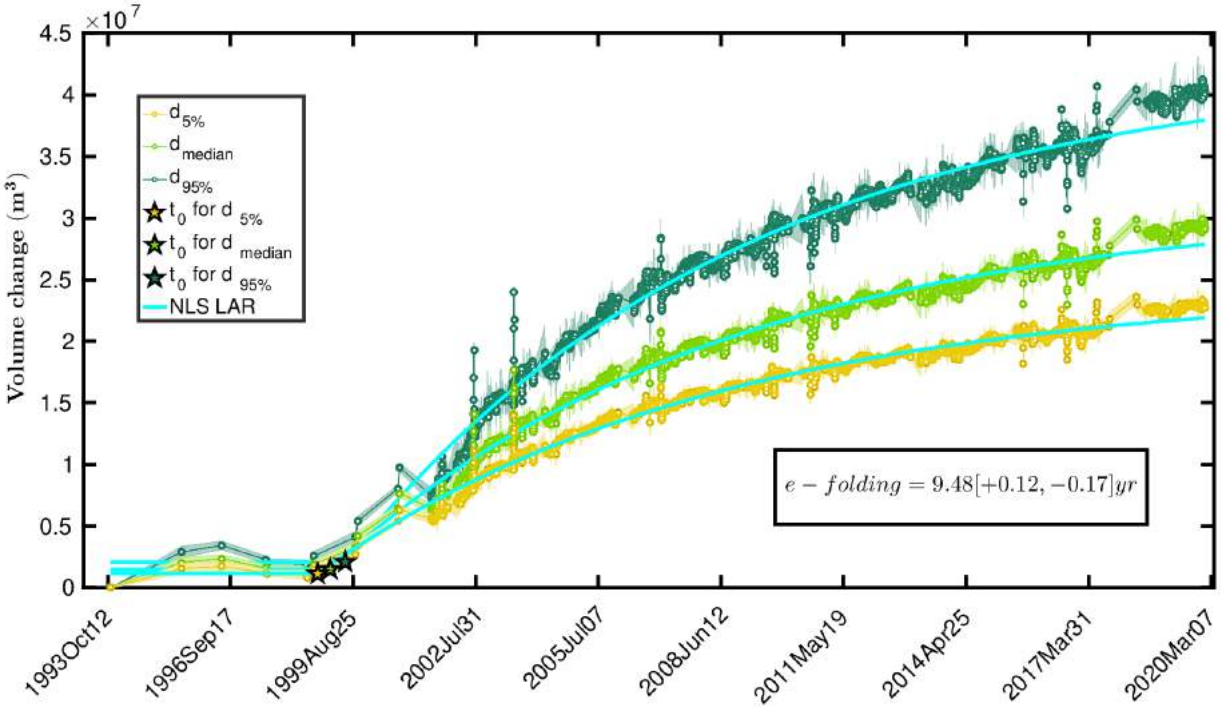

Figure 10. Volume change time series for a Mogi source (constrained by both the GPS and InSAR data), at different depth estimations (Table 1): median value (light green), 95% and 5% percentile values (yellow and dark green). Cian solid lines represent predicted curves through Non Linear Least Squares (NLS), Least Absolute Residuals (LAR) method, following the e-folding characteristic shape function of Equation 8. Stars show the location of the beginning of the exponential function: for data associated with median depth value estimation (light green), 95% and 5% percentile values (yellow and dark green).

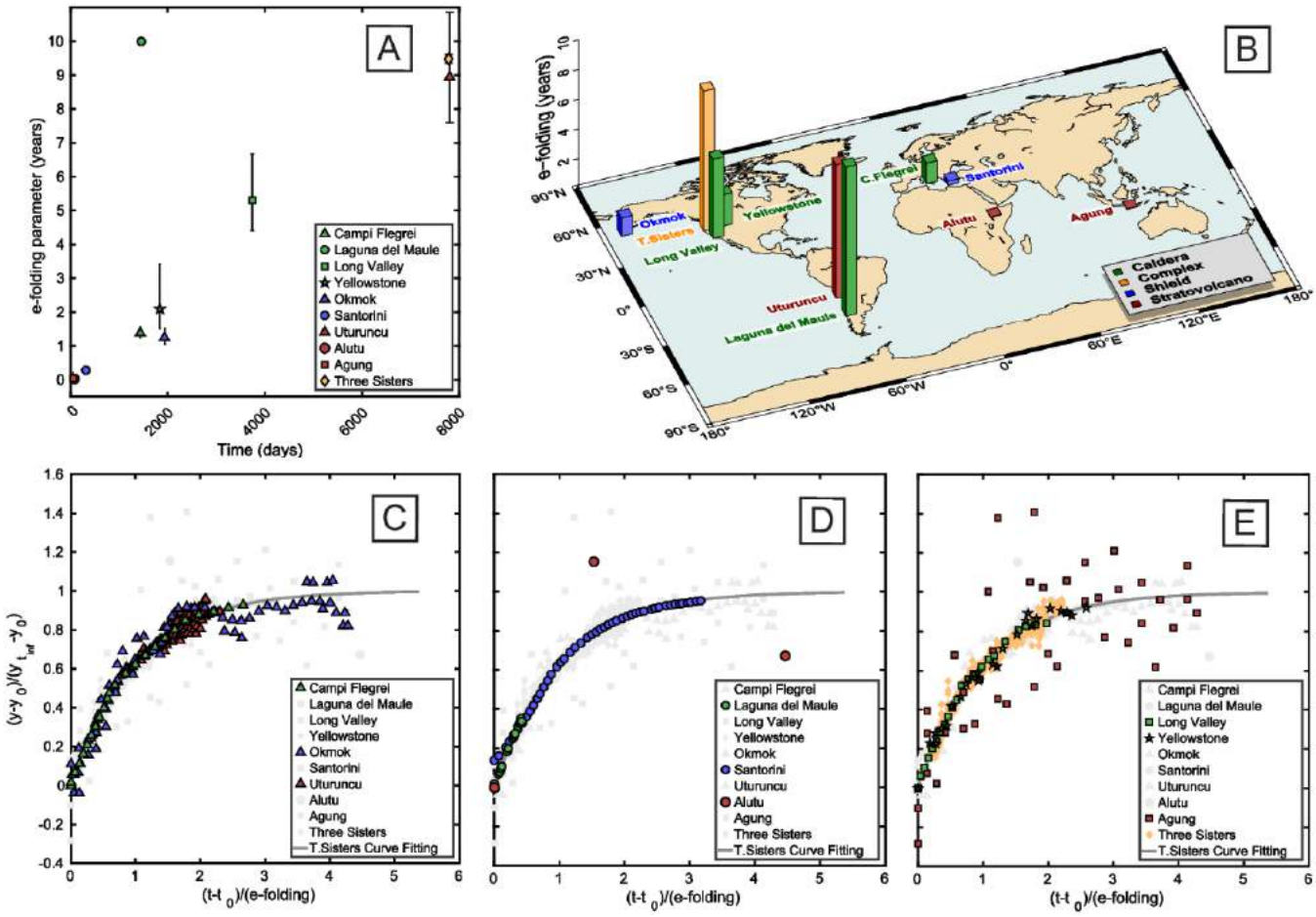

Figure 11. **(A)**: Estimated e-folding parameter of other available geodetic and volume time series from volcanoes with recent and well-studied unrest episodes: Okmok (Biggs et al., 2010), Long Valley (Hill et al., 2020), Uturuncu (Lau et al., 2018), Laguna del Maule (Le Mével et al., 2015), Yellowstone (Tizzani et al., 2015), Campi Flegrei (Troise et al., 2007), Santorini (Parks et al., 2015)), Alutu (Hutchison et al., 2016), Agung (Syahbana et al., 2019). **(B)**: Geographic location and classification according to the type of Volcano. **(C,E,F)**: Normalized uplift or volume change, y' (Equation 9) as function of normalized time, t' (Equation 10).

TABLES

Table 1. Prior information and Bayesian inversion results with the median a posterior probability solution and the 95% credible intervals, for the Elastic half-space Spherical Point Pressure deformation source (Mogi, 1958).

() Prior information.

	$X_{center}\,(m)$	$Y_{center}\,(m)$	$Depth\,(m)$	$\Delta V\,(10^6 m^3)$
Lower	-1.00×10^3	-1.00×10^3	5×10^2	0.1
Upper	1.50×10^4	1.50×10^4	2.00×10^4	1.00×10^4
Step	25	25	50	1.00×10^{-3}
Start	2.00×10^3	2.00×10^3	1.00×10^3	0.1

() Inversion results. Geo-reference point is $[-121.9, 44.03]\,degrees$.

	$Lon\,(degrees)$	$Lat\,(degrees)$	$Depth\,(m)$	$\Delta V\,(10^6 m^3)$
median	−121.8382	44.1055	5000	8.99
5%	−121.8418	44.1030	4500	6.98
95%	−121.8350	44.1082	6000	12.66

Table 2. Prior information and Bayesian inversion results with the median a posterior probability solution and the 95% credible intervals, for the Elastic half-space Penny-shaped sill-like source (Fialko et al., 2001).

() Prior information.

	$X_{center}\,(m)$	$Y_{center}\,(m)$	$Depth\,(m)$	$Radius\,(m)$	$\Delta P/\mu$
Lower	-1.00×10^3	-1.00×10^3	5×10^2	100	1×10^{-5}
Upper	1.50×10^4	1.50×10^4	2.00×10^4	4000	10
Step	25	25	50	50	1×10^{-6}
Start	2.00×10^3	2.00×10^3	1.00×10^3	100	1×10^{-2}

() Inversion results. Geo-reference point is $[-121.9, 44.03]\,degrees$.

	$Lon\,(degrees)$	$Lat\,(degrees)$	$Depth\,(m)$	$Radius\,(m)$	$\Delta P/\mu$
median	−121.8368	44.1018	6300	250	0.23
5%	−121.8398	44.0997	5600	220	0.05
95%	−121.8339	44.1041	7200	400	0.30

Table 3. Source location comparison for Three Sisters (assuming a Mogi source) from Previous Studies and the bayesian inversion carried out in this Study.

Inversion	$Depth\,(m)$	$\Delta V\,(10^6 m^3)$	$\Delta V_{rate}\,(10^6 m^3/yr)$
$1996-2000$, InSAR[(1)]	6500 ± 400	23.00 ± 3.00	$\sim 5.75 \pm 0.75$
$2001-2008$, Geodetic ground base data[(2)]	5800	22.20	~ 3.14
$1993-2008$, InSAR[(3)]	5200 ± 100	$57.00[+1.95, -3.60]$	$\sim 3.80[+0.13, -0.24]$
$1997-2000$, InSAR [This study][(4)]	$5000\,[+1000, -500]$	$8.99\,[+3.67, -2.01]$	$\sim 3.00[+1.22, -0.67]$

[(1)]ERS Descending (08/1996- 10/2000) (Wicks, 2002); [(2)]Campaign GPS, CGPS and Leveling (05/2001-late 2008) (Dzurisin et al., 2009); [(3)]ERS Track 385 Descending (08/1993-08/2008) (Riddick and Schmidt, 2011); [(4)]ERS Track 385 Descending (08/1997-09/2000).

Table 4. e-folding parameters obtained by NonLinear Least Squares, using the Least Absolute Residual method (LAR). Upper and lower bounds for the curve fitting parameters, encompassing the results for the volume changes series related to the 5%, median and 95% percentile values of source depth estimate.

Value	$c(yr^{-1})$	$1/c(yr)$	$t_0(yr)$	$R-square$	$RMSE$
optimal	0.1055	9.48	1999.09	0.989	0.60×10^6
lower bound	0.1042	9.60	1998.75	0.998	0.18×10^6
upper bound	0.1074	9.31	1999.59	0.988	0.87×10^6